Analysis of Damping From Vertical Sloshing in a SDOF System

L. Constantin, J. De Courcy, B. Titurus, T. Rendall, J.E.Cooper

Dept of Aerospace Engineering, University of Bristol

Abstract

The effect of the sloshing motion of liquid in a tank on the vertical transient motion of a single degree of freedom system is investigated. Step release tests of a vertically vibrating structure, including a tank containing liquid, demonstrate that added damping from the sloshing motion depends upon the amount of fluid in the tank and the maximum acceleration. The maximum amount of damping was observed at a 50% fill level and the system showed three distinct response regimes during the transient decay, all related to different motions of the fluid. The first response regime, immediately at the start of the transient, is considered to be the most important to exploit for aircraft gust loads alleviation due to its dominant role in the overall energy dissipation balance. Further, to advance the understanding of the modelling and predictive capabilities, coupled fluid-structure models of two opposing levels of fidelity were developed and evaluated. Namely, smoothed particle hydrodynamics (SPH) and an equivalent mechanical model (EMM) based on a bouncing ball model were considered to represent the fluid motion in the tank during the experiment. Both models are shown to provide good predictive capability in the initial impacting sloshing mode while the subsequent flow regime can be predicted with the SPH model only. The findings in this paper open routes towards improved coupled fluid-structure models and their use in improved aeroelastic wing design.

Keywords: Damping, Sloshing, Loads Alleviation, Experimental Rig Design

1. Introduction

There is a continuing drive to reduce the environmental impact of civil jet aircraft by improving performance through a decrease in fuel burn. This important goal can only be achieved through improving specific fuel consumption, the lift to drag ratio, flight/ground operations or reducing aircraft weight. All aircraft are subject to a range of different loads during flight and ground operations and these lead to the critical design cases which define the sizing, and hence the weight, of the aircraft structure [1]. One approach to achieve weight reduction is through the use of loads alleviation concepts to reduce the effect of turbulence, gusts and flight manoeuvres. Many different types of active and passive approaches have been used to achieve loads alleviation, including the conventional aerodynamic approach using control surfaces or spoilers whose motion is defined by an active control law related to the motion of the aircraft centre of gravity. Passive structural concepts are feasible but not yet widely implemented, including aeroelastic tailoring to couple the wing bending / torsion motions in a beneficial manner [2] and also the use of folding wingtips [3].

In the civil engineering field there have been many cases of using some form of fluid in a tank as a tuned mass damper to reduce the lateral response of tall buildings to the wind or earthquakes [4, 5]. Tuned mass dampers are relatively common in civil aircraft being used for instance to reduce the vibration and noise associated with engines [6] or aeroelastic response [7]. However, they tend to consist of mechanical systems rather than sloshing of a fluid in a tank, and have not been applied to gust or turbulence loads. With regard to damping in vertical vibratory systems, extensive work has been carried out on particle impact damping, where energy is dissipated through momentum exchange between particles of different sizes and the structure [9]. Vertically-excited systems containing liquids have also been studied previously, with applications such as liquid propellant tanks or water towers [10, 11, 12]. Relatively little work has considered such an approach for civil aircraft, with preliminary studies focused on numerical investigations on integration of fuel sloshing in aeroelastic models [8].

The use of *smoothed particle hydrodynamics* (SPH) and *equivalent mechanical model* (EMM) methods in fluid sloshing and fluid-structure interaction research is well established [41]. With the advent of high-performance computing, the use of detailed high fidelity SPH-based models for fluid sloshing problems is an attractive option. Alternatively, when in need of fast or large number of computations, such as for the optimum wing design, the use of low fidelity models might be preferred.

Smoothed particle hydrodynamics is a CFD technique based upon a Lagrangian description of fluid mechanics. Originally developed in 1977 by Lucy [24] and Gingold and Monaghan [25] for astrophysical problems, the method has seen widespread adoption in fluids dynamics. A fluid is discretised into a series of particles that are integrated through time and space, circumventing the need for a computational mesh and thus providing meshless advantages over the Eulerian methods. Most notable is the simplicity of modelling free surface flows, which usually require additional surface tracking techniques such as in the Volume of Fluid (VOF) method [26]. This benefit is significant when studying violent fluid sloshing as surface topology can be highly complex [39]. More generally, intricate geometries are more straightforward to model as the potentially challenging mesh generation process is simplified. Coupled with the strong conservation properties of a particle method, SPH is a highly applicable technique in many fields [27], including astrophysics and civil engineering. With the main focus on impact sloshing in the fixed wing aircraft fuel tanks, SPH is an ideal candidate to simulate this regime in the context of the laboratory experiment introduced in this research.

The use of EMM methodology in fluid sloshing problems has long history and was extensively described already in [10]. EMMs provide a simpler formulation of the dynamics of sloshing systems. An updated and comprehensive list of such approaches for modelling sloshing behaviour at the free surface in tank is offered by Ibrahim [18]. One of the first uses of EMMs in impact sloshing problems is presented in [40] and further addressed in [22, 20, 21]. There, a constrained mathematical pendulum swinging in the container was proposed to model hydrodynamic pressure impact arising from the free surface waves caused by the lateral oscillation of the container. A number of impact based EMMs that have been proposed and studied. In particular, this approach was used to study sloshing in the context of Liquefied Natural Gas carriers [42] and non-linear SDOF dynamics with strongly nonlinear sloshing by Farid & Gendelman [23]. Similar modelling approach and findings can be found in the field of vibro-impact particle-based damping systems as evidenced in the work of Friend & Kindra [9]. Nonlinear models are usually used in order to provide good representations of the lateral sloshing dynamics near resonances. However, the present paper is concerned primarily with the transversal out-of-plane dynamic interactions between a sloshing liquid and a tank. This situation leads to a problem formulation different in its nature compared to classically investigated sloshing systems. The experimental configuration used here enables measurements suitable to improve understanding of the damping originating from the fluid-structure interaction as well as a basis to evaluate EMM and SPH models in the well-defined test problem context.

SLOWD (sloshing wing dynamics) is an Airbus-led EU H2020 funded project that commenced in September 2019 to investigate the use of sloshing in aircraft wing fuel tanks to reduce the loading effects of gusts and turbulence. The project is aimed at developing fluid-structure interaction technologies to enhance the design of fuel tanks and their use such that loads reduction is achieved, leading to improved fuel efficiency and reduced environmental impact through structural weight savings. As part of this effort, some preliminary tests considered a cantilevered beam with attached water tanks subjected to vertical step-release transient excitation [15, 16]. It was found that the addition of the liquid increased the damping in the transient response, and that this damping was dependent upon the amount of liquid in the tanks. Although a good example of the possibility of exploiting fuel sloshing motion to impart added damping to aircraft wing motion, it was a difficult set-up for comparing the various fluid sloshing modelling capabilities being developed in the SLOWD project.

This paper describes experimental tests carried out on a nominally single degree of freedom (SDOF) vibratory system able to undergo step-release excitation. A rectangular tank, capable of being filled with liquid was attached to the beam structure. The focus is on vertical impact sloshing, as would be expected in aircraft wing gust response, and the effect that this has on the damping of the SDOF system's transient response. Transient tests were performed with different filling levels, and also different initial deformations, to assess their effect on the resulting damping levels. The vertical motion of the beam and tank was measured using an accelerometer, whilst a high-speed camera was used

to observe the fluid motion in the tank. It is intended that this relatively simple test set-up will provide a good basis for comparison with numerical modelling methods. Novel aspects of the work include development of the experimental rig (the T-beam), the experimental procedure and the focus on vertical impact sloshing. Comparison of the experimental results is made with two modelling approaches of different fidelities, *smoothed particle hydrodynamics* (SPH) and an *equivalent mechanical model* (EMM) based upon a bouncing ball model. These two models of opposing level of fidelity are used to assess the established methods and their predictive potential on this challenging fluid-structure interaction problem in otherwise well-defined and sufficiently controllable test configuration.

This paper is organised as follows: section 2 contains a description of the novel test rig, its performance and test campaign. Section 3 presents results and analysis of two sets of experiments that were performed. Sections 4 and 5 introduce the SPH and EMM models that were developed. The comparisons between the experiments and predicted results are summarized in section 6. Finally, conclusions and future research directions are provided in section 7.

Nomenclature

β	Newmark coefficient
Δt	Time discretisation
Δu	Spatial discretisation
γ	Adiabatic index, Newmark coefficient
μ	Mass ratio between bouncing ball and structure
ν	Kinematic viscosity
ω	Angular frequency
ω_d	Damped natural frequency
ω_n	Undamped natural frequency
ρ	Density
ρ_w	Density of water
σ_w	Surface tension of water in contact with air
env	Envelope function
ζ	Damping ratio
ζ_d	Damping ratio of dry structure
ζ_w	Damping ratio of wet structure
ζ^e_{w1}	Experimental damping
ζ^m_{w1}	EMM damping
A	Fourier transform of acceleration signal
$a(t)$	Acceleration signal
a_0	Initial acceleration amplitude
A_H	Fourier transform of Hilbert transform of acceleration signal
a_H	Hilbert transform of acceleration signal
A_I	Imaginary part of Fourier transform of acceleration signal
A_R	Real part of Fourier transform of acceleration signal
c	Speed of sound
d	Depth of tank
E	Young's modulus
F	Fitness function
f	Frequency
f^E	Experimental frequency
f^T	Theoretical frequency
g	Gravitational acceleration
h	Height of tank, SPH smoothing length
h_L	Liquid column height
I, V	Sets used for event identification
i, j	Particle indices
K	Stiffness constant
k	Iteration number
k_1	Wavenumber of the first symmetric sloshing mode
k_{max}	Maximum iteration number
L	Length of tank
m, M	Mass
M_{eq}	1DOF equivalent mass
n	Time index

P	Pressure	u_{b0}	Initial displacement of ball
R	Coefficient of restitution	v_0	Initial velocity of tank
t	Time coordinate	v_{b0}	Initial velocity of ball
$u(t)$	Displacement signal of tank	W	Weighing function, SPH kernel function
u_0, A_0	Initial displacement of tank	x, y, z	Cartesian coordinates
$u_b(t)$	Displacement signal of ball		

2. Experimental set-up

The driver behind the test configuration and experimental approach was to develop a novel well-defined linear, lightly damped 1DOF structure where the vertical sloshing behaviour could be examined in a controlled and repeatable manner. Such a configuration aims to represent the motion of aircraft wings subjected to atmospheric turbulence or landing loads, where the vibration response primarily consists of the first bending mode. The chosen experimental arrangement comprises of a "T-beam" type structure with well separated lightly damped modes and a tank containing water attached to the mid-point of the horizontal beam. Transient excitation was applied via a static point load, using a turnbuckle at the centre of the horizontal beam, to achieve pre-defined deflections before a sudden release. The vertical acceleration of the top of the tank was measured with an accelerometer and the fluid motion recorded using a high speed camera.

2.1. Experimental Rig

A schematic with the main dimensions (in mm) of the structure and a photo of the test set up can be seen in figures 1 and 2 where two beams are attached together to form a T joint (hereafter referred to as *T-beam*), and the three ends are all clamped. The z axis is the vertical axis - the direction of initial deflection. Axes x and y form the horizontal plane of the tank.

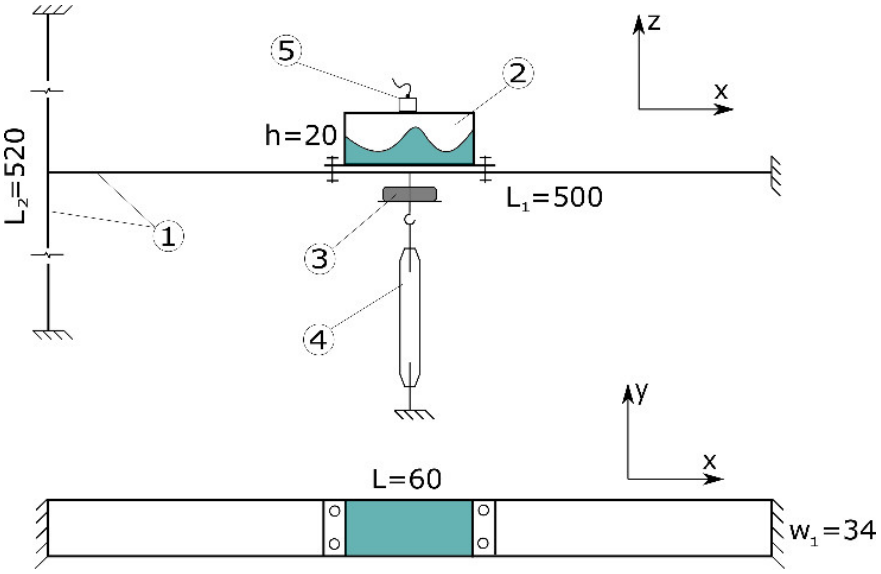

Figure 1: Schematic of T-Beam structure

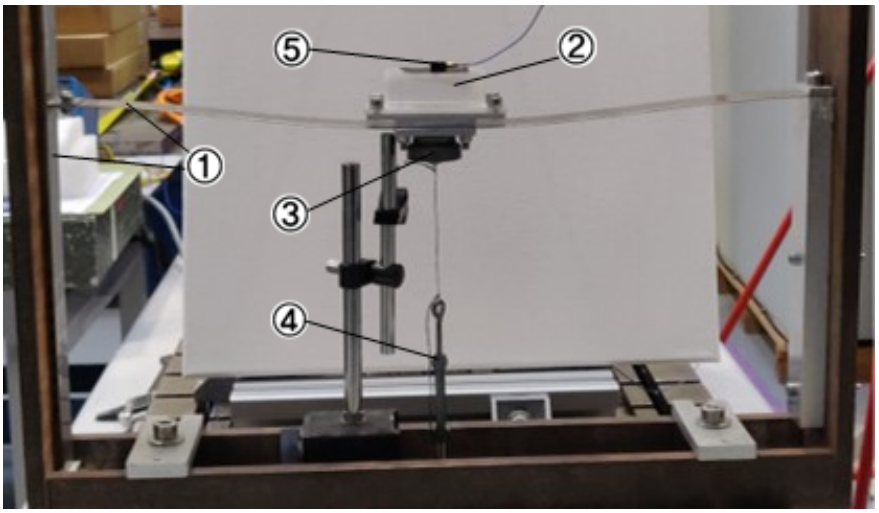

Figure 2: Photo of T-Beam structure

The test setup consists of the following main components, annotated in figures 1 and 2:

1. Stainless steel beams of thickness of 1 mm, width $w_1 = 34$ mm and lengths $L_1 = 500$ mm and $L_2 = 520$ mm respectively.
2. Acrylic tank containing tap water at the room temperature with width $L = 60$ mm, height $h = 20$ mm, depth $d = 30$ mm. The tank is positioned at the middle of the beam, which is the point of minimum lateral motion of the tank. Geometric nonlinearities, as well as asymmetry in the boundary conditions of the horizontal beam can lead to slight changes in this optimum position, but this was not studied in this research.
3. Added mass attached below the tank of 0 to 36 grams, depending on the volume of water in the tank, so that the total mass at the centre of the beam remains constant (see table 1).
4. Turnbuckle used to load the system to the required initial deformed configuration.
5. Accelerometer placed at the centre of the tank ceiling to measure the vertical acceleration (z axis) with the recorded signal sampled at 2048 Hz.
6. High speed camera aimed horizontally to the tank to record the fluid motion to enable visual assessment of the flow conditions.

Unlike a single beam cantilevered at its both ends, which can experience non-linear stiffening effects when the central out of plane displacements reach values higher than the thickness of the beam, the T-beam structure is found not to experience any significant non-linearity in the loading range of interest. This design characteristic is due to the T-junction being able to rotate around the y axis and also move along the x axis in a less restricted way compared to the overconstrained doubly-cantilevered configuration. Figure 3 demonstrates that the static linearity of the tank deflections resulting from forces up to 16 N extends up to at least 14 mm (14 times the thickness of the horizontal beam) with the measured stiffness found as $K = 1.1$ N/mm.

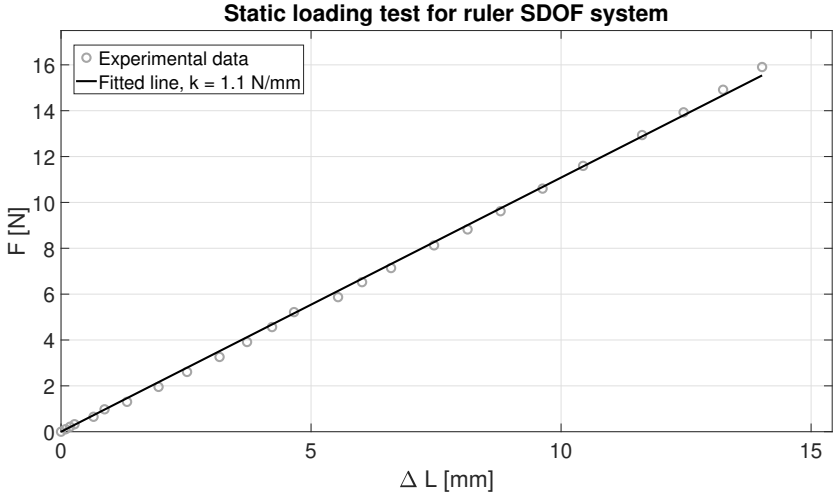

Figure 3: Static deflection of tank for the loading applied in the z-direction

2.2. Test Methodology

Two different sets of experiments were performed to systematically investigate the effect on the sloshing behaviour when varying the filling level in the tank and also when increasing the initial deformation before the step-release.

2.2.1. Varying Filling Level

The aim of the first set of tests was to explore the effect of different tank filling levels on the transient response whilst maintaining the same initial deformation. The beam was pulled downwards by a chord attached to the turn-buckle so that an accurate and repeatable amount of deflection (14 mm in all the cases considered here) was possible. The transient response was recorded once the chord was cut. The total mass of the system was kept constant by attaching the tuning weights underneath the tank. Table 1 shows how the damped natural frequency of the system remains relatively unaffected for all levels of fluid in the tank, with an overall variation between -0.1% and 0.2% .

Exp No.	Water Level (%)	Water Mass (g)	Added Mass (g)	Total Mass (g)	Freq (Hz)
1.1	0	0	36	36	10.05
1.2	10	3.6	32.4	36	10.06
1.3	20	7.2	28.8	36	10.04
1.4	30	10.8	25.2	36	10.05
1.5	40	14.4	21.6	36	10.05
1.6	50	18	18	36	10.05
1.7	60	21.6	14.4	36	10.07
1.8	70	25.2	10.8	36	10.05
1.9	80	28.8	7.2	36	10.05
1.10	90	32.4	3.6	36	10.04
1.11	100	36	0	36	10.05

Table 1: Parameters for filling level variation test cases

2.2.2. Varying Initial Deflection

The second set of tests considered the effect of changing the initial displacement between 1 mm and 14 mm, and hence the maximum acceleration experienced (up to $7m/s^2$), before the system was released. These tests were repeated for three different water fill levels: 30%, 50% and 70%. Table 2 shows the different parameter combinations that were considered.

Exp No.	Water Level (%)	Initial Deflection (mm)	Max Acceleration (g)
2.1.1-3	30/50/70	1	0.46
2.2.1-3	30/50/70	2	0.94
2.3.1-3	30/50/70	3	1.49
2.4.1-3	30/50/70	4	1.80
2.5.1-3	30/50/70	5	2.18
2.6.1-3	30/50/70	6	2.73
2.7.1-3	30/50/70	7	3.32
2.8.1-3	30/50/70	8	4.35
2.9.1-3	30/50/70	9	4.33
2.10.1-3	30/50/70	10	5.02
2.11.1-3	30/50/70	11	5.29
2.12.1-3	30/50/70	12	5.92
2.13.1-3	30/50/70	13	6.21
2.13.1-3	30/50/70	14	6.94

Table 2: Parameter combinations when varying the initial deflection

3. Experimental Results

The experimental results are presented in this section, first focusing on the 50% filling level case and initial amplitude of 14 mm in order to investigate the characteristic response and damping behaviour of the coupled beam-tank system. Then, the variation of damping trends with the filling level and peak acceleration is considered. Selected tests were conducted three times to ensure repeatability of the test results, especially for all the dry structure cases (with no fluid inside the tank) and 50% filling level cases (where the influence of the fluid on the system was found to be maximized). The test responses were found to be sufficiently repeatable giving a high degree of confidence in the completed experimental investigation.

3.1. Characteristic Response

Figure 4 provides a qualitative view of a typical acceleration time series, and also the variation of the system's frequency in time, for the dry and 50% filling level test cases. A marked difference (increased damping) in the decaying time responses can be seen when the fluid is introduced to the system. This influence is particularly noticeable during the first part of the coupled system's response. Further, the two acceleration signals present small shifts in their phase difference as they evolve in time due to the slight frequency fluctuations observed mainly in the second part of the response, see figure 4. These changes are considered minor and are thought to be caused by slight nonlinearities present in the dry structure and additional high frequency effects that are found to have negligible influence in this study. The frequency changes in time were computed by fitting a short-window decaying harmonic function on the sliding window lasting six full periods of the processed signals [16]. The maximum deviation from the measured mean value of 10.05 Hz is 1.5% and thus the frequency of the system can be considered to be stable in time.

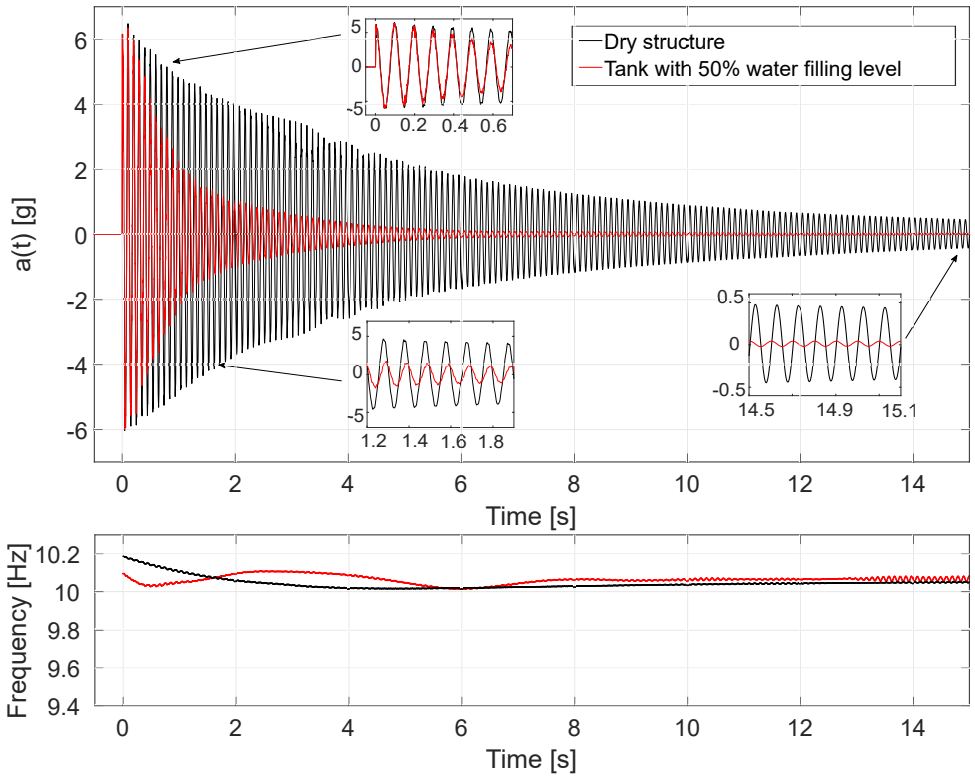

Figure 4: Tank vertical acceleration and frequency changes for dry and 50% full cases

Given that the T-shape experimental rig was designed to produce a lightly damped single degree of freedom system at low frequencies, the frequency content of the system needed to be evaluated in the $0-100$ Hz range to evaluate how well these goals had been achieved. The response of the system in the relevant frequency range was studied using two tools. The *Fourier Transform* was applied to the entire dry case step-release acceleration data to investigate the global frequency response levels of the system and to identify all frequencies present in the response to a step release test. A *Wavelet Transform* (WT) analysis was also performed to observe the system's frequency behaviour localised in time and to investigate any possible nonlinear effects which might be apparent through frequency variation in time.

The frequency spectrum is represented in figure 5, with normalized vertical axis. Inspection of the frequency spectrum illustrates the dominant single degree of freedom behaviour of the system in the frequency range of interest. There are a number of harmonics present in the dry system's response, but these are much smaller than the response at the first bending mode of the structure at 10.05 Hz. The second harmonic at 20.1 Hz has a response magnitude of only 2% of the response observed on the first mode. All higher harmonics of the fundamental frequency are assumed to have negligible participation on the system's response within the range of the applied step-release inputs.

The wavelet transform of the acceleration data for the dry case was obtained using the *Wavelet Toolbox* in MATLAB ver. R2019a and is presented in figure 6. As with the Fourier analysis, the wavelet spectrum indicates no other major frequency present in the system at any time; moreover, there is no significant frequency change in time, which is consistent with the frequency analysis presented in figure 4 and indicates linearity in the dynamic behaviour of the system.

Both these results demonstrate that, for the purpose of studying sloshing-induced damping via vertical step-release excitation, the experimental rig exhibits sufficiently linear and single degree of freedom behaviour.

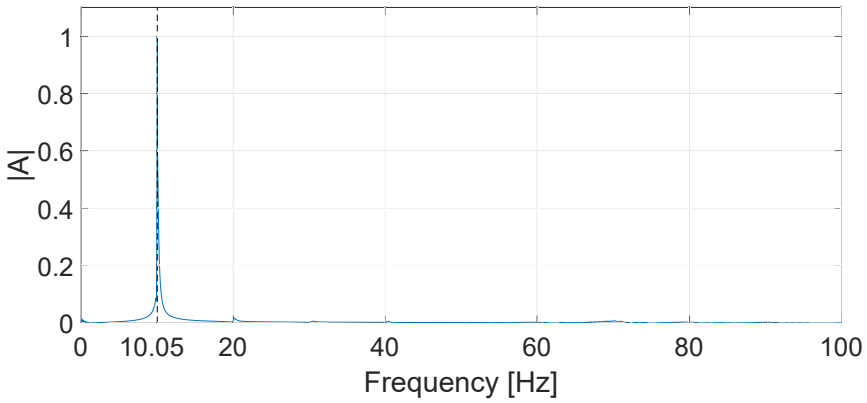

Figure 5: Amplitude - Frequency characteristic of the dry system

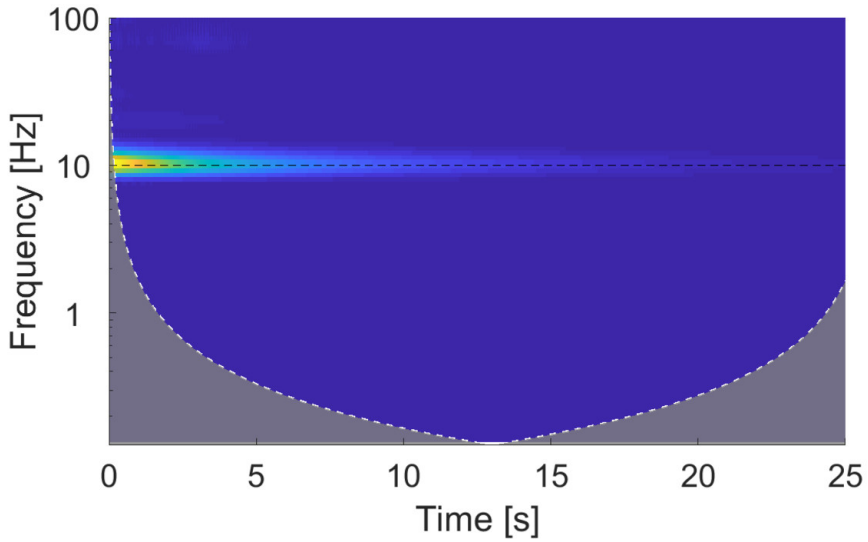

Figure 6: WT spectrum of the dry system

As we are dealing with a SDOF system, the damping characteristics of the time responses can be obtained by plotting the acceleration data on a logarithmic scale. For linear SDOF systems with viscous damping, which are characterised by exponential decay in their free response, joining the maximum values of each oscillation of the acceleration will give a straight line on a logarithmic scale from which the damping can be easily found [19]. Previous results [16] show that the envelope of the log plots of acceleration data can be used to identify damping trends in the system, even when the damping in the system is controlled by the time-varying sloshing-induced dissipation mechanism. There are multiple ways of extracting the signal envelope. The Hilbert transform is a suitable tool for constructing the envelope function of systems which display single degree of freedom behaviour, such as the one analyzed here. The procedure used to construct the envelope function using the Hilbert transform is described in [13, 14].

Using this envelope identification procedure, the sloshing-induced damping is found to be piece-wise linear, as seen in figure 7, which is shown when plotting the logarithm of the acceleration envelope against time. This transient response shows three distinct damping regions with nearly constant rate of exponential decay. They will be referred to from now on as R1, R2 and R3. Each of the regions correspond to different behaviours of the fluid inside the tank. The

approach was found to provide a useful insight into the changing nature of the fluid-induced damping mechanisms inherent in the system.

An example of the results obtained using this type of analysis is presented in figure 7, where the logarithm of the envelope function is plotted against time. There is a "ripple" on these curves which are characteristic of such an envelope computation and also the effects of noise; these "ripples" are exaggerated by the logarithmic scale at very low amplitudes. It can be seen that the dry case can be approximated by a weakly bi-linear damping response, with two regions of $\zeta_{d1} = 0.34\%$ and $\zeta_{d2} = 0.23\%$, respectively. This slightly nonlinear behaviour, potentially due to the behaviour of the structure's joints at different deflection levels, is also thought to be associated with the shifts in the frequency shown in figure 4. The difference in the dry damping levels in the two regions is very small compared to the changes in the wet case, as seen in figure 7. The underlying damping of the dry structure is low and so from a damping point of view the T-shape rig is suitable for the study of sloshing-induced damping.

The 50 % fill case shows three distinct regions, which can be assumed to occur in a linear piece-wise fashion, with damping ratios of $\zeta_{w1} = 1.76\%$ (R1), $\zeta_{w2} = 0.87\%$ (R2) and $\zeta_{w3} = 0.22\%$ (R3). These results confirm the findings of [15] and [16] in that the sloshing induces additional energy dissipation in the coupled fluid-structure system compared to the zero fill cases, and that a number of piece-wise linear sections occur which are acceleration amplitude dependent. It is this fundamental observation that constitutes the key approach taken in both the qualitative and quantitative analyses of the selected test configurations.

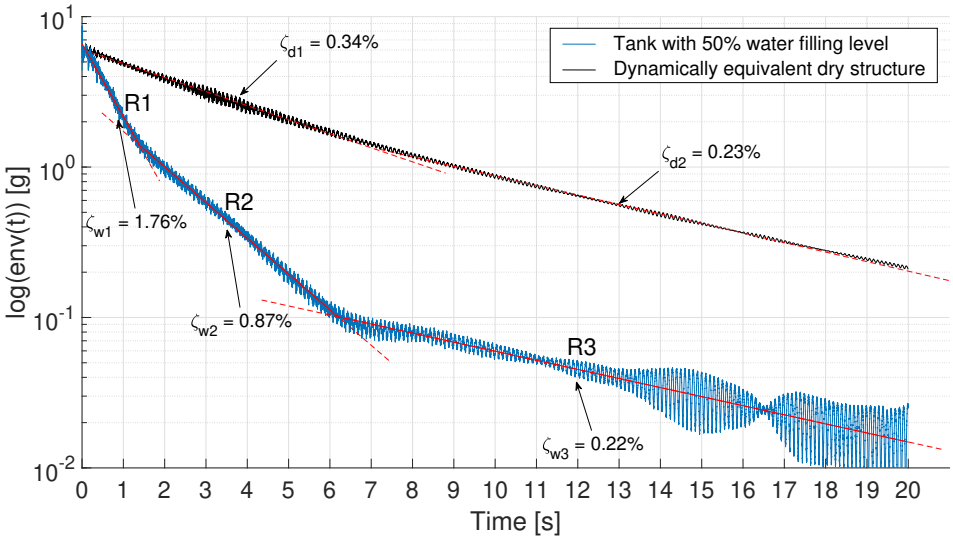

Figure 7: Logarithm of acceleration time response envelope of dry and 50% sloshing case

Further insight can be gained by examining the fluid behaviour corresponding to the different sections of the response. Figure 8 contains multiple experimentally recorded snapshots of the fluid motion with each row showing three characteristic images from one of the damping regions. Each of these three regions shows distinct fluid behaviour:

- Region R1 is the region associated with the highest level of damping and corresponds to a very turbulent fluid motion with the fluid impacting both the floor and ceiling of the tank. The damping mechanism appears to be associated with repeated impacts between the fluid and the tank. As this region also corresponds to the largest displacements and accelerations, it is considered that this regime will be the most important for exploitation of any potential loads alleviation for aircraft wings.
- Region R2 is characterised by the fluid motion of the first symmetric sloshing mode in a rectangular tank, described in detail in the literature [17, 18]. Occasional impacts with the ceiling of the tank happen, although

they are not comparable in magnitude to the impacts seen in R1. The frequency of the first symmetric sloshing mode can be determined analytically [17] as

$$\omega_1^2 = \left(gk_1 + \frac{\sigma_w}{\rho_w}k_1^3\right)\tanh(k_1 h_L) \tag{1}$$

where L is the length of the tank, $k_1 = 2\pi/L$, g is the gravitational acceleration, $\sigma_w = 7.28 \cdot 10^{-2}$ N/m is the surface tension of water in contact with air at an ambient temperature of 20° C, ρ_w is the density of water and h_L is the height of the water column ($h_L = h/2$ for 50% filling level). In this case, a theoretical value for the first symmetric sloshing mode frequency of $f_{w1}^T = 4.7$ Hz is obtained, which compares well with the experimental value of $f_{w1}^E = 5$ Hz determined by inspection of the high-speed camera footage. It should also be noted that the frequency of this lateral sloshing motion is half the frequency of the vertical vibration of the system, corresponding to previous investigations that have found that under parametric excitation of a frequency close to twice the natural frequency of a certain sloshing mode, the liquid free surface will oscillate exhibiting the shape of that mode [17, 18]. Energy is thus extracted from the oscillating system to maintain the motion of the first symmetric sloshing mode, resulting in a damping ratio of $\zeta_{w2} = 0.85\%$ for the 50% filling level case.

- Region R3 shows very little motion of the fluid inside the tank. Although similar to the fluid behaviour seen in R2, the amplitude of the motion of the system during R3 is of the order of 0.1 mm so this region of the system response is not influenced by the fluid motion. Consequently it possesses the damping, $\zeta_{d2} = 0.22\%$, strongly dominated by the underlying damping of the second section of the dry structure response.

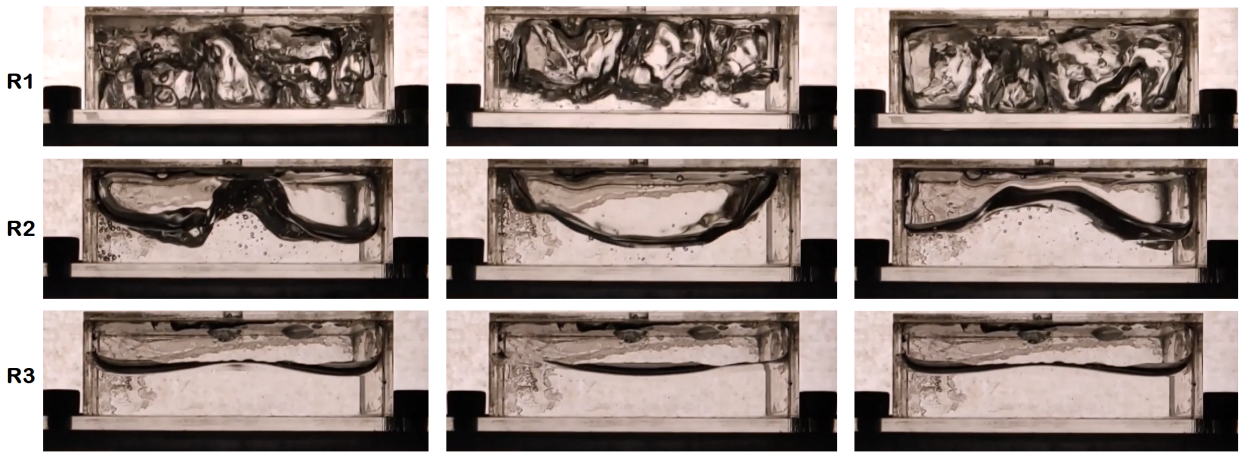

Figure 8: Representative photos of the sloshing motion for the three characteristic damping regions

The main focus of this paper will be on the R1 region as this provides the dominant damping mechanism for the largest motions, and corresponding loads, of the system. For the 50% filling level case that is considered here, the range of deflections in R1 is between 14 mm and 2 mm. The liquid was found to have negligible influence at the lowest amplitudes.

3.2. Study 1: Effect of filling level

The effect of filling level on the sloshing-induced damping is investigated by varying the filling level whilst keeping the initial amplitude constant at 14 mm, using the parameters defined in table 1.

A summary of all the damping trends obtained is presented in figure 9. It shows the damping ratios estimated in each region and for each filling level as described in figure 7. The dry structure damping values, essentially equal to

the damping in R3, are also shown using red lines. An automated procedure for damping region identification was put in place to ensure that no bias was introduced in the process, and this approach was used for identifying the damping values for all of the data presented in this work. The *Curve Fitting Toolbox* in MATLAB ver. R2019a was used to find the best piece-wise linear fit function over the log of the envelope in least-squares sense (using the *lsqcurvefit* implementation).

As explained before, three damping regions were identified for all filling levels and the corresponding damping value calculated from the slope of the fitted envelope function on a logarithmic scale. The sloshing-induced damping effect is found to be maximized at 50% filling level, consistent with previous findings. Titurus *et al.* [16] reported similar behaviour in a sloshing beam experiment, where the damping was also found to be piece-wise linear and maximized at 50% filling level. The damping in the second region R2 is found to be substantially smaller and it does not follow the same clear trend with the filling level. Considering the correlation between the fluid sloshing mode and the measured damping ratio, inevitable variations in the sloshing motion lead to variations in the measured R2 damping ratio. Moreover, as seen in equation 1, the sloshing frequency of the fluid varies as a function of filling level, further influencing the damping ratio in this region. Typical R2 results are presented here and supplementary studies focused on R2 are needed to confidently assess the influence of all the phenomena contributing to the R2 sloshing-induced damping. The R3 damping is found to be very low overall and close to the underlying damping of the dry structure. This finding is consistent with the qualitative behaviour of the fluid observed in Figure 8, namely that in region R3 the fluid contributes very little to the system's energy dissipation.

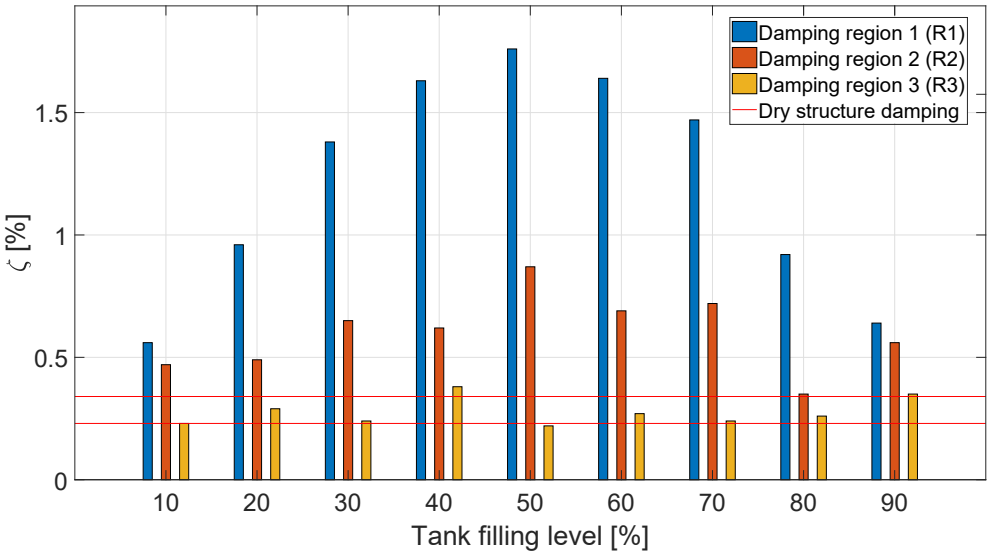

Figure 9: Damping in the three characteristic regions vs fluid filling level

3.3. Study 2: The effect of excitation level

The effect of excitation level (or maximum acceleration level) on sloshing-induced damping is assessed by varying the peak acceleration, via different initial deflections, for three different filling levels (30, 50 and 70% respectively) using the parameters shown in table 2.

Consider the logarithm of the the system acceleration envelope function plotted against time for different levels of maximum acceleration, obtained by varying the initial displacements, as shown in figure 10 for the 50% fill level case. The acceleration envelopes, computed using the Hilbert transform, are stacked vertically and labeled with the corresponding dimensionless excitation level (a_0/g) to facilitate easy comparison. Guiding red lines are drawn to highlight the damping trends in different damping regions.

At a minimum excitation level of 0.46 g, the damping in the system is essentially the underlying damping of the dry structure, as the liquid is not moving substantially inside the tank. As the excitation level increases (0.94 g – 1.49 g curves in figure 10), a build-up zone approximately 10 cycles long is formed in which the fluid activity increases. The fluid then transitions into motion pattern associated with the R2 region described in section 3. At acceleration levels 1.80 g and 2.18 g the initial build-up region is less discernible and only one region of damping ratio, $\zeta = 0.87\%$ and $\zeta = 0.76\%$ respectively, was identified. For excitation levels $\geq a_0 = 2.73\ g$, the motion is large enough to introduce substantial impacts between the fluid and the tank's top and bottom surfaces leading to an increase in the damping levels.

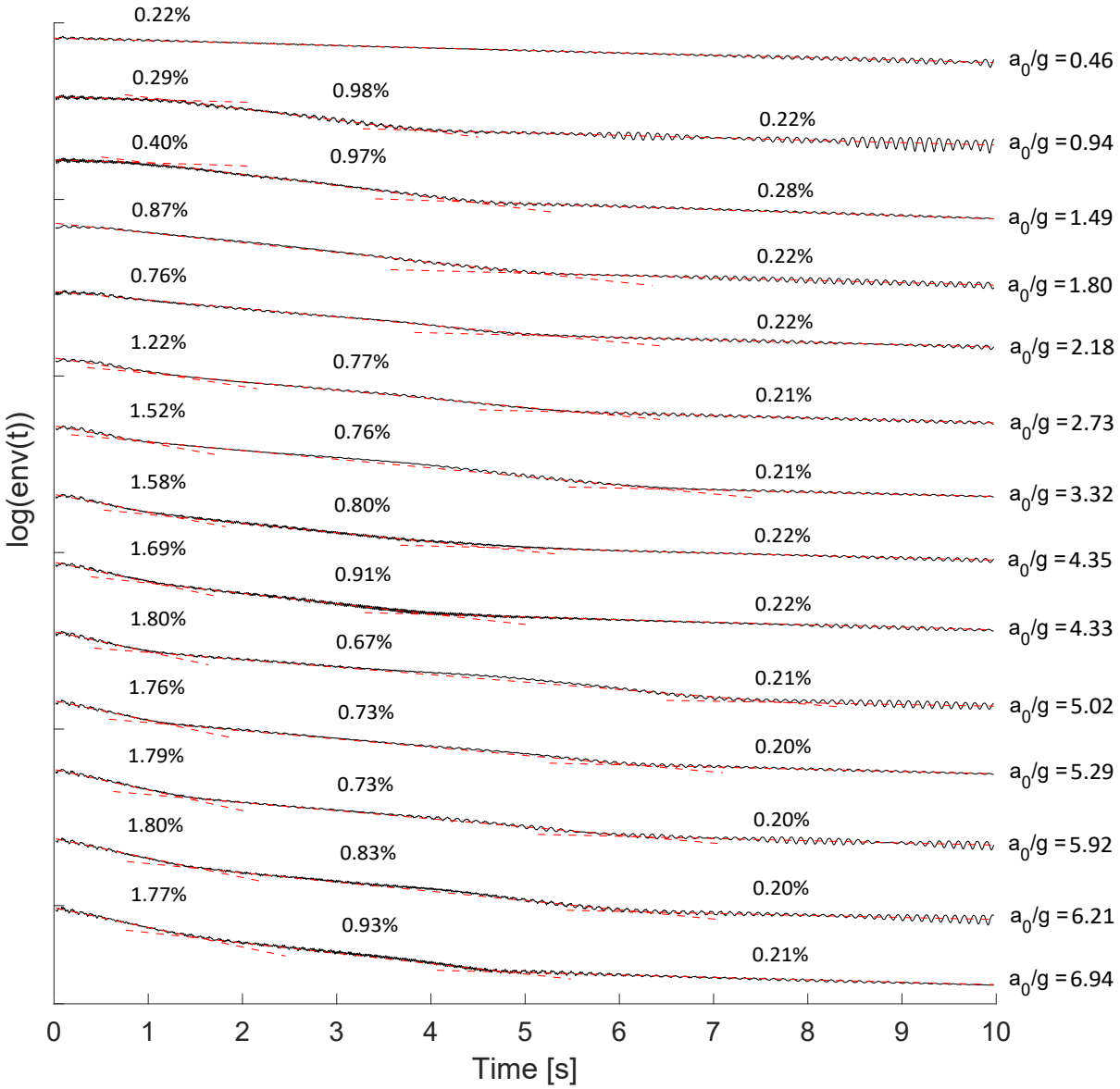

Figure 10: Envelope function for 50% fill case and different maximum acceleration levels

The data presented in figure 10 and the delineation between different damping regimes can be better understood by examining the damping map shown in figure 11 which describes the evolution of damping trends with time and

their dependency on initial acceleration. The isolines between the three characteristic damping regions, obtained by fitting the approximating polynomials to the identified acceleration envelopes from figure 10, are set to $\zeta = 0.35\%$ and $\zeta = 1.2\%$. The two small white regions present in figure 11 at low excitation levels indicate non-physical values of damping arising from the local overfitting effects and, due to their inconsequential nature, are neglected in further analysis.

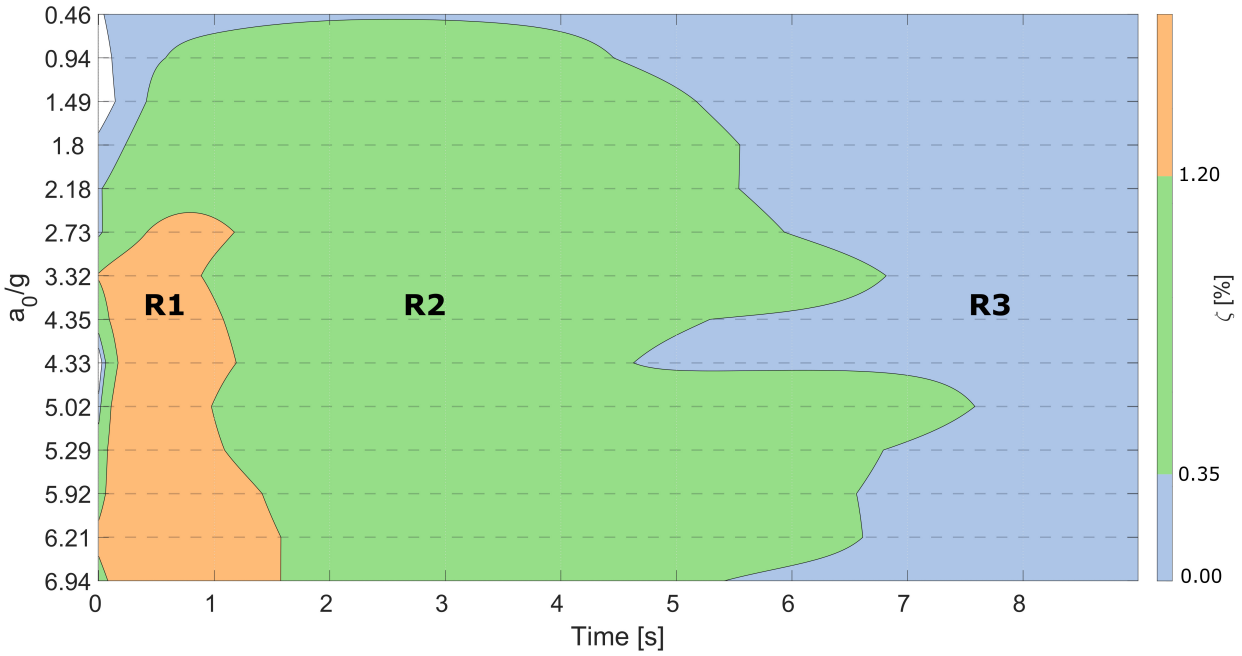

Figure 11: Damping ratio map $\zeta(a_0, t)$ for 50 % filling level

The zones represented in figure 11 define where the system displays the behaviour described in subsection 3.1. The timestamps defining the regions correspond to the intersection points between the guiding red lines in figure 10. As detailed before, region R1 represents the motion at high excitation levels where turbulent vertical sloshing motion takes place; comparatively, R2 area is a more extended region in time, closely associated with the horizontal motion of the liquid. It occurs when the acceleration levels are low enough such that no turbulent vertical motion is present. Finally, R3 region emerges during low amplitude motions. From the damping point of view, it leads to the responses which are, in effect, indistinguishable from the dry structure's motion. Furthermore, a zone with the high damping ratio gradient can also be observed at the start of R1. This where the system quickly evolves from the rest, i.e. zero damping at $t = 0$ s, to the R1 sloshing regime. As in figure 10, a fluid motion build-up region is evident at low excitation levels (top left corner in figure 11) and it reduces in size as the excitation level increases.

Further, based on figures 10 and 11, it is important to note that after a certain maximum acceleration threshold, around 3.3 g, increase in the sloshing-induced damping capacity saturates and the damping ratio levels off to almost a constant value. This finding is best seen in figure 12 where the damping level corresponding to the first response regime R1 is plotted as function of excitation level. The damping trends for the 30%, 50% and 70% fill level cases are compared; as in figure 9 it can be seen that the R1 damping levels for the 30% and 70% filling levels are similar. A piece-wise linear function was fitted over the R1 damping vs maximum acceleration data. The two linear regions are thus established and similar slopes are obtained for all three filling levels. The line corresponding to the higher excitation levels has a considerably lower slope compared to that at a lower excitation. The damping ratio thus only increases slightly after the acceleration threshold is reached. It follows that slightly more energy is absorbed in the R1 region as the maximum acceleration level goes past the 3.3 g threshold.

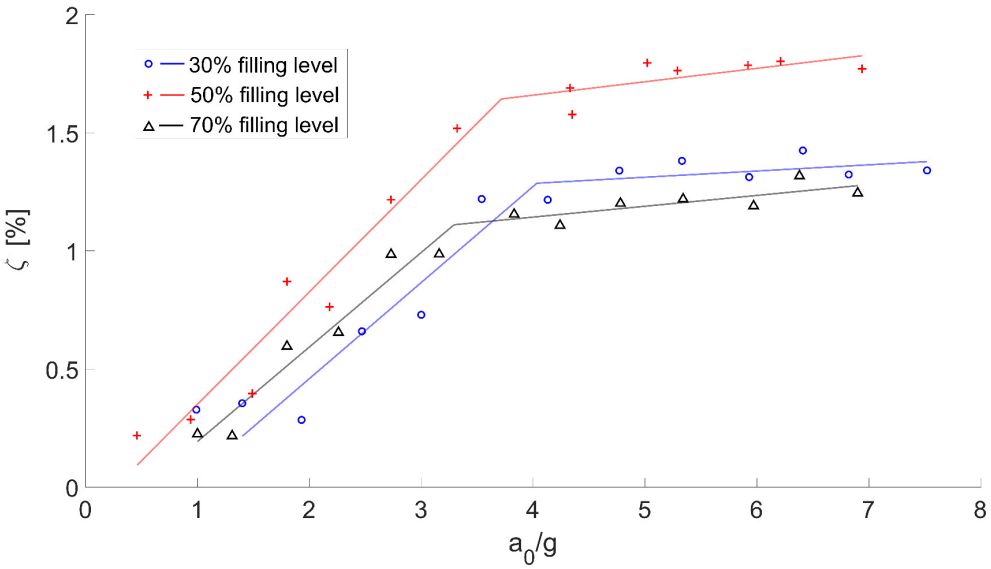

Figure 12: R1 damping level vs maximum acceleration

Two different models of varying complexity are built based on the presented experimental results in order to gain a better understanding of sloshing-induced damping mechanisms and to assess their predictive capability. These models are discussed in the following sections.

4. Single DOF Model with SPH fluid sloshing

4.1. SPH Formulation

Within this section the formulation of SPH is summarised; the fundamental idea is to approximate any arbitrary function as a smoothed summation over a neighbourhood of scattered points or particles. This interpolation can be applied to the equations of motion of choice, and particles integrated forward accordingly. With fluid dynamics being the matter at hand, the initial objective is to approximate the pressure gradient within inviscid flow ($D\boldsymbol{v}/Dt = -\nabla P/\rho$). Two approaches can be followed, one formulation derives the equations of motion directly from the Lagrangian, as detailed by Price [28]. The alternate method is subsequently detailed, and approximates a function as a weighted summation over a neighbourhood of particles [29]. Kernel interpolation theory begins by considering the integral representation of an arbitrary variable A through a volume Ω in the form

$$A(\boldsymbol{x}) = \int_{\Omega} A(\boldsymbol{x}')\delta(\boldsymbol{x} - \boldsymbol{x}')d\boldsymbol{x}', \tag{2}$$

where δ is the Dirac-delta function and $d\boldsymbol{x}$ a volume element. Equation 2 is an exact interpolation, but cannot be integrated, hence the delta function is replaced with a smoothing function $W(\boldsymbol{x} - \boldsymbol{x}', h)$ such that

$$< A(\boldsymbol{x}) >= \int_{\Omega} A(\boldsymbol{x}')W(\boldsymbol{x} - \boldsymbol{x}', h)d\boldsymbol{x}'. \tag{3}$$

The smoothing or kernel function W has a radius of influence proportional to a length scale h, termed the 'smoothing length'. As the kernel function is only an approximation of the delta function, equation 3 cannot be exact, but is second order accurate if W is symmetric and meets the normalisation condition $\int_x W d\boldsymbol{x} = 1$ [28]. Hence, this step is defined by the kernel approximation operator <>. Similarly, the spatial derivative can be approximated by replacing $A(\boldsymbol{x})$ with $\nabla A(\boldsymbol{x})$, and with some modification results in

$$< \nabla A(\boldsymbol{x}) >= -\int_{\Omega} A(\boldsymbol{x}')[\nabla W(\boldsymbol{x} - \boldsymbol{x}', h)]d\boldsymbol{x}', \tag{4}$$

for details of this process see [29]. Ultimately, the gradient can be evaluated purely from A and the kernel derivative, equivalent operators are available for divergence and curl of a vector field. However, equation 4 is only strictly true when the kernel support is entirely within the problem domain, truncation of the kernel support from boundaries or free surfaces introduces error.

With the continuous fluid being discretised by a finite number of particles, the integral in equations 3 and 4 can be approximated by a summation over N neighbouring particles, which are assigned mass and density, taking the form

$$< A(\boldsymbol{x}_i) > \approx \sum_j^N A(\boldsymbol{x}_j) W(\boldsymbol{x_i} - \boldsymbol{x_j}, h) \frac{m_j}{\rho_j}, \tag{5}$$

$$< \nabla A(\boldsymbol{x}_i) > \approx - \sum_j^N A(\boldsymbol{x}_j) \nabla W(\boldsymbol{x_i} - \boldsymbol{x_j}, h) \frac{m_j}{\rho_j}. \tag{6}$$

Equation 5 represents the SPH particle approximation of a variable or function. A fundamental application of SPH is to set $A(\boldsymbol{x})$ equal to $\rho(\boldsymbol{x})$, deriving the SPH density estimator

$$< \rho(\boldsymbol{x}_i) > = \sum_j^N m_j W(\boldsymbol{x_i} - \boldsymbol{x_j}, h). \tag{7}$$

With the particle approximation, the equations governing particle motion for fluid flow can now be formulated; initially consider the inviscid momentum equation from the Lagrangian perspective such that

$$\frac{D\boldsymbol{v}}{Dt} = -\frac{\nabla P}{\rho} + g. \tag{8}$$

The kernel approximation operator is subsequently dropped for clarity. Equation 8 can be directly evaluated using the particle approximation, but results in a term that does not conserve linear nor angular momentum [30]. Thus, to symmetrise the pressure gradient the identity

$$\frac{\nabla P}{\rho} = \nabla \frac{P}{\rho} + \frac{P}{\rho^2} \nabla \rho \tag{9}$$

is applied, leading to

$$\frac{\nabla P}{\rho} = - \sum_j^N \frac{m_j}{\rho_j} \left[\frac{P_j}{\rho_j} \right] \nabla_i W_{ij} - \left[\frac{P_i}{\rho_i^2} \right] \sum_j^N \frac{m_j}{\rho_j} \rho_j \nabla_i W_{ij} = - \sum_j^N m_j \left[\frac{P_j}{\rho_j^2} + \frac{P_i}{\rho_i^2} \right] \nabla_i W_{ij}. \tag{10}$$

Equation 10 is the most common form of the pressure gradient used in SPH, but alternate formulations are available [28]. The complete SPH formulation used within this work is

$$\frac{D\boldsymbol{v}_i}{Dt} = - \sum_j^N m_j \left[\frac{P_j}{\rho_j^2} + \frac{P_i}{\rho_i^2} \right] \nabla_i W_{ij} + \sum_j^N m_j \nu \frac{\rho_i + \rho_j}{\rho_i \rho_j} \frac{\boldsymbol{x}_{ij} \cdot \nabla_i W_{ij}}{|\boldsymbol{x}_{ij}|^2 + 0.001 h^2} \boldsymbol{v}_{ij} + \boldsymbol{g}, \tag{11}$$

$$\frac{D\rho_i}{Dt} = \sum_j^N m_j \left[\boldsymbol{v}_{ij} + \boldsymbol{n}_{ij} \left(\frac{c_{i,j}}{\rho_j} (\rho_j - \rho_i) \right) \right] \cdot \nabla_i W_{ij}, \tag{12}$$

$$P = \frac{\rho_0 c_0^2}{\gamma} \left[\left(\frac{\rho}{\rho_0} \right)^\gamma - 1 \right], \tag{13}$$

$$W_{ij} = \alpha_d \left(1 - \frac{|\boldsymbol{x}_{ij}|}{2h} \right)_+^4 \left(\frac{2|\boldsymbol{x}_{ij}|}{h} + 1 \right). \tag{14}$$

Note, $x_{ij} = x_i - x_j$ and the equivalent for velocity v_{ij}. Equation 11 is the chosen momentum formulation, where the additional second term is a laminar viscosity [31]. Equation 12 is used to evolve the densities of particles rather than set them according to equation 7 as this performs better in the vicinity of free surfaces where a particle's neighbourhood is not complete. The density rate of change includes a term analogous to a Rusanov flux [32], reducing noise in the density and pressure fields. A variation of Tait's equation of state (equation 13) is used to evaluate particle pressures without having to solve a pressure Poisson equation, where γ is usually set to 7 for water [34]. c_0 (the numerical speed of sound) is chosen to be 10 times the largest expected velocity [35], rather than the true value for water to permit a larger time step. Using this stiff equation of state can accurately resolve free surfaces, and is generally known as the weakly compressible SPH method (WCSPH). Wendland's quintic kernel (equation 14) is used for the smoothing function [36]; this provides sufficient smoothness for the equations of motions and good computational efficiency. Wendland's kernels have also been shown to avoid the particle pairing instability in SPH [37]. α_d is a normalisation factor, equal to $7/4\pi h^2$ and $21/16\pi h^3$ in two and three dimensions, respectively.

Numerous methods for boundary conditions have been developed in SPH, most commonly applying repulsive forces derived from Leonard-Jones potential within the support radius of a boundary. In this work dynamic boundary particles are employed [33], these particles line the boundary with pressures evolving according to equations 12 and 13 to repel fluid from leaving the domain. The simplicity of this method has strong advantages in fluid-structure interaction (FSI) problems, as the velocity and displacement of the structure can be mapped onto the boundary particles to enforce boundary motion. Additionally, force from the fluid acting upon the boundary can be calculated simply from

$$\boldsymbol{F}_i = m_i \frac{D\boldsymbol{v}_i}{Dt} \tag{15}$$

and interpolated onto the structural model or summed across all boundary particles to define a global force.

Time integration is performed implicitly using the Newmark-beta method [38]. Particle acceleration (equation 11) and density rate of change (equation 12) are substituted into equations 16 and 17, and fixed point iteration performed until particles have converged at the subsequent timestep (n+1). γ and β are set to $1/2$ and $1/4$, respectively; giving the unconditionally stable, constant average acceleration method.

$$\dot{\boldsymbol{x}}^{n+1} = \dot{\boldsymbol{x}}^n + (1-\gamma)\Delta t\ddot{\boldsymbol{x}}^n + \gamma\Delta t\ddot{\boldsymbol{x}}^{n+1} \tag{16}$$

$$\boldsymbol{x}^{n+1} = \boldsymbol{x}^n + \Delta t\dot{\boldsymbol{x}}^n + (0.5-\beta)\Delta t^2\ddot{\boldsymbol{x}}^n + \beta\Delta t^2\ddot{\boldsymbol{x}}^{n+1} \tag{17}$$

4.2. Fluid-Structure Coupled Model

A partitioned approach to fluid-structure coupled simulation is employed here, allowing the fluid and structural domains to be solved independently and coupled together through force and displacement exchange. Specialised solvers can thus be used for each domain, preferable over a monolithic approach which would require inclusion of the structural physics directly into the SPH formulation. Any form of structural representation can thus be chosen to represent the T-beam, as long as the formulation is capable of receiving force from the fluid, returning displacement information, and a similar temporal discretisation to ensure time synchronisation.

With the structural system designed to perform nominally as a single degree of freedom system, the dry structure is represented as

$$M\ddot{x} + C_1\dot{x} + C_2\dot{x}|\dot{x}| + Kx = F_{fluid} - Mg \tag{18}$$

A velocity-squared damping term was introduced to enable a better approximation of the experimental, as well as the assumed, bi-linear damping response within the range of interest. Despite having little effect on the dry dynamics, the weight of the structure is included here. This is to ensure the tendency toward a steady-state deflection of the coupled system is correct, as the SPH will inherently induce a deflection from particle weight. F_{fluid} is the force calculated from the components of the SPH fluid equation 15 in the direction of motion summed across all boundary particles.

Parameters describing the T-Beam structure are given in table 3, where the stiffness and mass were determined experimentally based on the results presented in section 2. The mass value M shown is for the 50% filling level, hence it includes the added mass (18 g) but not the fluid mass (18 g). For varying fill levels, the added mass is set to ensure total mass remains at 276 g. To determine the two damping parameters of the dry structure an optimisation was performed, matching the numerical response of equation 18 directly to the envelope of the experimentally recorded acceleration data.

M	$258g$
K	$1.1\ N/mm$
C_1	$0.074\ Ns/m$
C_2	$0.099\ Ns^2/m^2$

Table 3: T-Beam structural parameters used in SDOF-SPH coupled model (50% fill case).

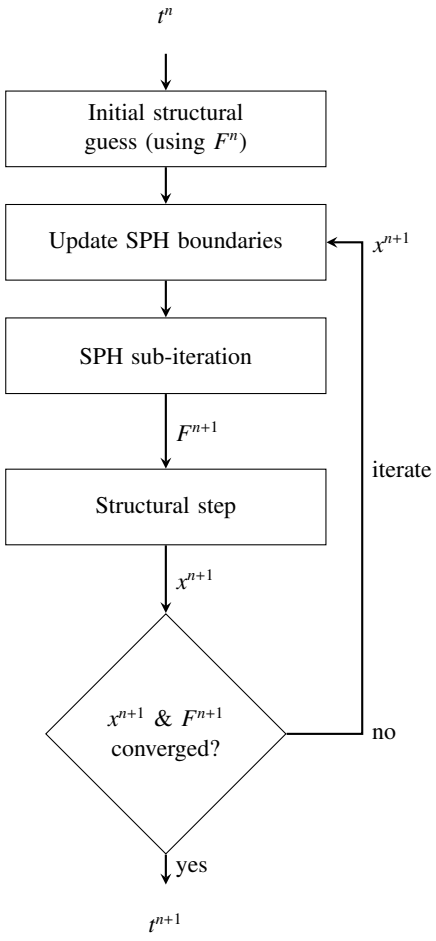

Figure 13: SPH-structure coupling technique.

Conservation of energy within the fluid-structure system is vital, as the sloshing problem at hand represents a complex exchange of energy between the structural and fluid dynamics. Coupling of the partitioned solvers is therefore performed using a strong (or tight) coupling methodology, as described in figure 13. Sub-iteration of the two solvers

is performed to synchronise the domains at the subsequent timestep, which ensures an energy-conserving coupling. The solution is assumed converged when the change in displacement and fluid force between iterations is below a set tolerance, effectively requiring the work-done by the fluid and thus energy transfer to be consistent.

4.3. Computational Setup

For the following SPH study, all fluid parameters were set to that of water and thus no calibration was required; kinematic viscosity $\nu = 8.9 \cdot 10^{-7}\ m^2/s$ and rest density $\rho_0 = 1000\ kg/m^3$. The numerical speed of sound c_0 was set to $50\ m/s$ for all simulations, which is sufficiently high to maintain stability during violent sloshing. Compact support of the particles is set such that the smoothing length is twice the initial inter-particle spacing, and the time-step tailored to ensure sufficient stability. Particles are initialised in a Cartesian grid, according to the internal dimensions of the tank and chosen fill-level. A hydrostatic pressure gradient is set and meniscus prescribed to replicate steady-state fluid conditions before release, as shown in figure 14.

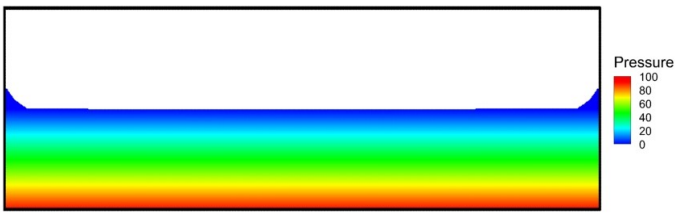

Figure 14: Particle initial conditions. Contour level is pressure in Pascals.

4.3.1. Resolution Requirement

Initial simulations were run to determine the particle resolution required to adequately resolve the first sloshing regime R1; to ensure the dominant energy dissipation mechanisms in the fluid are replicated without unnecessary computational overhead. These simulation were run for the 50% fill and highest experimental deflection, as this case maximised the R1 damping response; which is assumed to exhibit the most intricate physical behaviour. Table 4 shows the series of resolutions assessed, where $L/\Delta x$ defines the initial number of particles across the length of the tank and Δt the required timestep. These resolutions relate to particle numbers of roughly 600 to 60 thousand for the 50% fill case.

The nominal damping value is calculated in the same manner as for the experimental data, by automatically fitting a piece-wise linear function through the logarithmic envelopes. Acceleration responses are shown in figure 15. A clear curvature emerges within the response envelopes, both within R1 and the transition into R2, which introduces some uncertainty when considering the assumed linear fit. Thus, to introduce a measure of variation, a second-order polynomial is also fitted to data in R1 region and the maximum and minimum gradients are extracted to define boundaries on ζ_{w1}.

$L/\Delta x$	$\Delta t\ [\mu s]$	ζ_{w1} [%]
60	20	0.97 (0.93 - 1.02)
120	5.0	1.36 (1.34 - 1.38)
300	2.0	1.61 (1.29 - 1.93)
400	1.0	1.77 (1.15 - 2.33)
600	0.8	1.74 (1.55 - 1.89)
Experimental		1.73

Table 4: Effect of SPH resolution on the damping in R1 region.

Initially, considering the nominal damping values in table 4, as expected there is a clear increase in correlation between the SPH and experimental response with increasing spatial resolution. However, the bounds on the estimated

damping remain significant as a result of the deviation from the constant slope assumption. Furthermore, there exists no significant inflection point into R2, and in fact the existence of a second regime is questionable itself for all resolutions. This observation is discussed further in section 6.1). Therefore, by assessing the computed results, the 300-particle case was gauged as satisfactory for resolving the first sloshing regime, whilst minimising the computational overhead. This resolution is thus used for all of the following SPH simulations.

Another notable observation is that despite the varying spatial resolution, all considered cases converge onto an almost identical final response at around 5 s in figure 15. This implies the same amount of energy is dissipated by the fluid in each case, just at a different rate. A less violent response of the fluid would thus be expected for the coarser cases, which is indeed what was observed. This can mostly be attributed to the larger particles having an increased support radius; thus a greater proportion of the fluid particles includes the boundary within their stencil. Bulk motion of the fluid is therefore more influenced by the structure than the fluid dynamics itself, ultimately leading to reduced particle velocities relative to the tank and 'softer' impacts. Ultimately, this is an effect of the boundary discretisation and not the SPH formulation itself, and is simply resolved by choosing a sufficiently fine resolution as done previously.

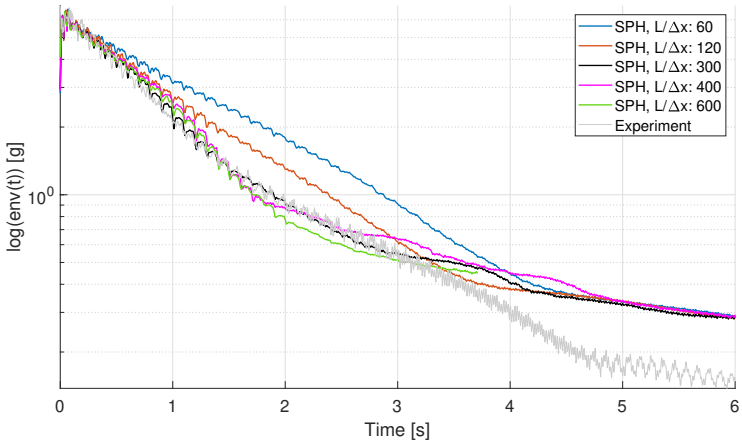

Figure 15: SPH acceleration response (50% fill case) for the varying resolutions defined in table 4.

5. Single DOF Model with EMM fluid sloshing

5.1. Description of the EMM

Based on experimentally observed behaviour, this work uses a phenomenological EMM where a simple linear spring-damper-mass oscillator is combined with a single free ball contained and interacting with the upper and lower boundary of the oscillating system's mass. A schematic of the system can be seen in figure 16. The spring-damper-mass part of the model represents the T-structure with the tank, with mass M, stiffness K and damping coefficient c. The ball in this model represents the fluid during its vertical R1 sloshing stage; while classically referred to as *bouncing ball*, in this case it behaves as a *bouncing rigid body* with its height h_L depending on the water filling level and it is represented in figure 16 as the rigid bars above and below the ball. The ball is either in free-flight or it undergoes an instantaneous inelastic impact with the structure dependent on the chosen coefficient of restitution. As opposed to the previous SPH model where a weak quadratic dry damping nonlinearity was used to avoid discontinuities, a linear representation of the T-structure is adopted here in order to be able to implement the model in the following computationally-efficient semi-analytical form.

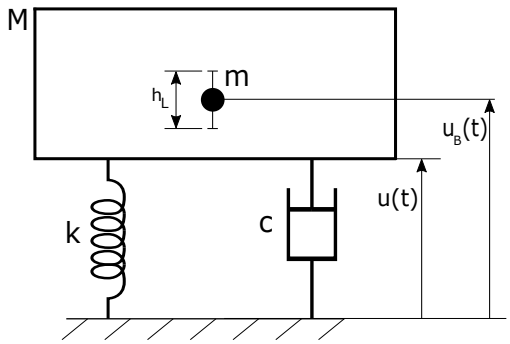

Figure 16: Schematic of equivalent mechanical model

The equations governing the dynamics of the EMM are based on the formulation for a vibrating single degree of freedom system with viscous damping and a point mass falling under gravity. The equations are classically solved analytically, but impact events between the ball and the tank must be identified and accounted for accordingly. In order to enable impact identification, a discretised form of the equations is used such that

$$u(k+1) = e^{-\zeta\omega_n\Delta t}(u_0 \cos\omega_d\Delta t + \frac{v_0 + \zeta\omega_n u_0}{\omega_d}\sin\omega_d\Delta t) \tag{19}$$

$$u_b(k+1) = u_{b0} + v_{b0}\Delta t + \frac{1}{2}g(\Delta t)^2 \tag{20}$$

Here, the subscript b indicates the ball model. The quantities with subscript 0 are initial conditions dependent on the previous iteration. Equation 19 is represented in a form that makes the use of a known initial displacement and velocity of the system. The two expressions for the vibrating tank and the bouncing ball essentially represent the complete description of the EMM. The impact condition between the vibrating mass and ball determines the post-impact initial conditions which are applied to equations 19 and 20. The interaction between the two systems is implemented using a coefficient of restitution R which, together with the equation of conservation of momentum, leads to the contact condition formulated in terms of velocities [9] defined as

$$\begin{aligned} v(k+1) &= \frac{v_b(k)\mu(1+R) + v(k)(1-\mu R)}{1+\mu} \\ v_b(k+1) &= \frac{v_b(k)\mu(\mu-R) + v(k)(1+R)}{1+\mu} \\ \text{when } u(k) + h - \frac{h_L}{2} - \Delta u \le u_b(k) &\le u(k) + \frac{h_L}{2} + \Delta u \end{aligned} \tag{21}$$

where μ is the mass ratio between the ball and the structure. In equations 21 the Δt and Δu represent the time and spatial discretisations, respectively. The coefficient of restitution is defined such that a value of $R = 1$ represents perfectly elastic impact.

For the purpose of this investigation, the system is implemented using *MATLAB ver. R2019a* and a flowchart describing the implementation is presented in figure 17.

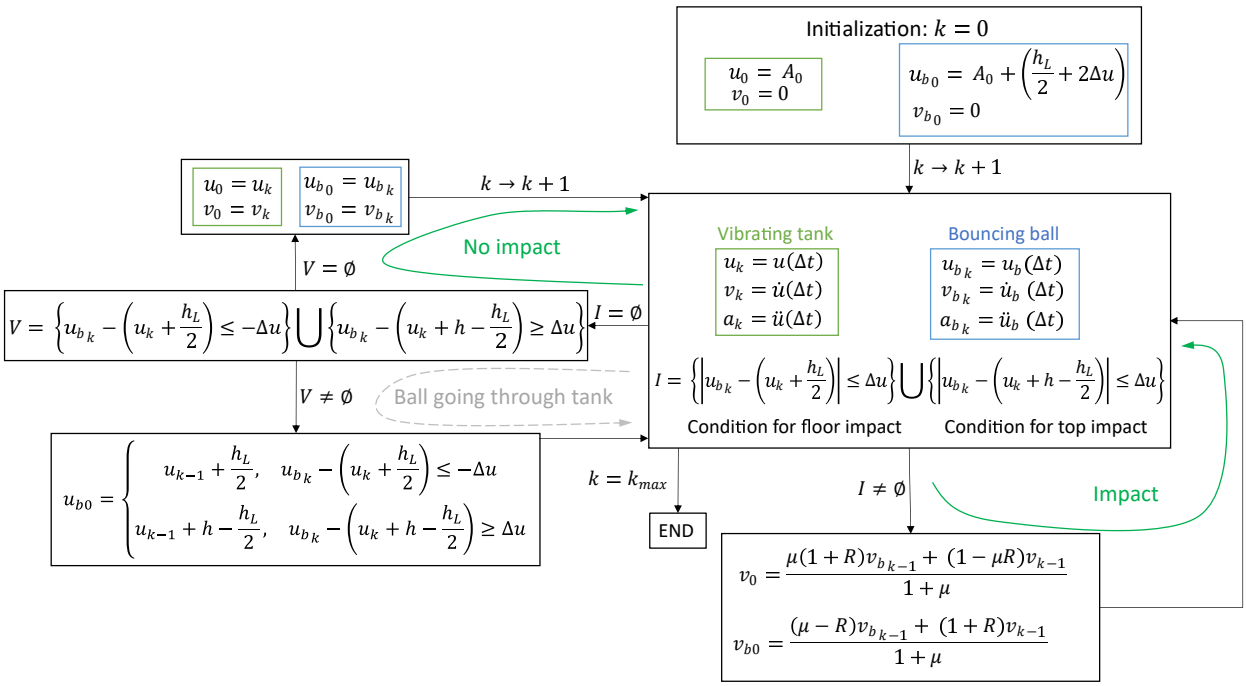

Figure 17: Flowchart of equivalent mechanical model implementation

A time discretisation of $\Delta t = 10^{-6}\ s$ and a spacial discretisation of $\Delta u = 10^{-6}\ m$ are used, providing suitable resolution for this problem. The system is initialized using the known initial amplitude (A_0) and velocity ($v_0 = 0\ m/s$) of the tank. The bouncing ball starts from the bottom of the tank at rest; two distance units Δu are imposed between the tank and the ball initially, as a way of ensuring that the impact condition does not need to be enforced in the first iteration; this is a measure taken to avoid numerical errors in the first iteration and it does not affect in any substantial way the behaviour of the system. After initializing the system, the iteration number is advanced and the algorithm enters the main block in figure 17, where equations 19, 20 and their corresponding derivatives are evaluated. The impact condition is assessed by means of the set I which mathematically describes the spatial coincidence of the two bodies within the spatial tolerance Δu. If the set I is not empty it implies that either the condition for impact with the floor or with the top of the tank is reached. The algorithm continues by not advancing the iteration number but imposing the conditions in equations 21, effectively changing the velocity initial conditions according to the coefficient of restitution and conservation of momentum.

If no impact event is detected, the initial conditions are updated with the information obtained at the current iteration and the iteration number is advanced (left-hand side of diagram in figure 17). There is, however, an intermediate step represented by the evaluation of set V. The definition of the coefficient of restitution implies a change in initial velocities when an impact is detected. The initial velocities are changed depending on the velocities at the previous iteration, which can get low enough such that the ball isn't allowed to *bounce* back. This phenomenon thus happens at the end of the relative motion between the ball and the tank, when the ball goes through the wall of the tank. To provide correction and ensure the stability of the model, a supplementary condition is verified, represented by the set V. If the set V is empty, it means that the ball is inside the tank, no impact has been detected and the algorithm advances up on the chart, as described previously. If, on the other hand, the set V is not empty, it means that the ball is out of the tank. The iteration number is not advanced and instead a correction is provided by imposing a coincidence condition between the ball and the tank. The discretisations used, Δt and Δu, ensure that the behaviour of the algorithm is not affected in any significant way by introducing this correction. The algorithm stops when the maximum iteration number (k_{max}) is reached; this number depends on the desired simulation time.

The physical quantities used for the model are chosen depending on the system to be modeled, as follows:

- Mass of the liquid inside the tank m is directly proportional to the filling level; the mass of the liquid at 100% filling level is $36g$.
- Mass of the tank M is the equivalent single degree of freedom mass of the T-shape rig ($M_{eq} = 276g$) minus the mass of the liquid.
- The stiffness of the system is evaluated experimentally at $K = 1100\ N/m$ (Figure 3).
- The underlying structural damping of the system is set according to the experimental results for the dry structure: $\zeta = 0.23\%$ when $a \leq 2\ g$ and $\zeta = 0.34\%$ otherwise. The end result of using an acceleration-dependent damping ratio, which for a given oscillation frequency is equivalent to imposing a displacement or velocity-dependent damping conditions, is comparable to that achieved by introducing the nonlinear damping term in the SPH model formulation (equation 18), while allowing for a straightforward analytical formulation of the problem (Equations 19 and 20).

5.2. Tuning of the EMM

The behaviour of the model is dictated by the initial conditions, physical characteristics of the system, as well as the coefficient of restitution. The initial conditions and the physical characteristics are defined by the modeled system and have been presented in the previous subsection. Depending on the value of R, the amount of momentum transferred between the tank and the ball at each impact changes, thus affecting the level of effective damping observed in the vibrating system. The coefficient of restitution is thus the tunable parameter in the model.

Due to the nature of the model presented, the only damping regions the model is capable of describing are R1 and, trivially, R3. The second region of damping, as emphasized in subsection 3.1, is strongly correlated with the first symmetric sloshing mode of the liquid inside the tank, hence with the lateral dynamics of the liquid. The model tuning was thus done in such a way as to minimize the difference between the experimental R1 damping and the damping obtained numerically. However, the two sets of data are not directly comparable by fitting lines over the identified regions as described in subsection 3.2. An example of an acceleration envelope obtained for a coefficient of restitution of $R = 0.51308$ at 50% filling level is presented in figure 18, where a deviation from linearity in R1 damping is observed. This behaviour was found to be correlated with the coefficient of restitution itself, where lower values of R lead to lower deviations from damping linearity and higher levels of damping. A straight line fitted through the acceleration data in R1 is thus not sufficient to fully describe the R1 damping behaviour in the case of the EMM. Instead, second degree polynomials are used to approximate R1 damping rates in the logarithmic scale. Then, for the following comparisons, the varying damping value in R1 is derived from the slope of the fitted parabola. For the sake of comparison with the experimental data, a mean value of the coefficient of restitution in R1 was used as a metric (e.g. figure 19). It should be noted that the same procedure was applied for the experimental and SPH data as well.

An in-house *Genetic Algorithm* was used to search for the optimum value of R by minimizing the difference in R1 damping relative to the experimental data presented in table 1 and figure 9. A discretisation of 1e-5 was used on the search space for R, a resolution that was found to be appropriate for the sensitivity of the model to changes in the coefficient of restitution. The difference in damping level is minimized in an L^1 sense, leading to the objective function

$$F = \sum_{i=1}^{9} W(i) \cdot \left| \zeta_{w1}^{e}(i) - \zeta_{w1}^{m}(i) \right| \tag{22}$$

Here, W is a weighing function equal to 2 for the filling levels 40% to 60% and 1 otherwise, providing a 2:1 weighing of the mid-range filling levels where the damping was experimentally found to be maximized. The superscripts e and m refer to the experimental and model data, respectively.

The optimum value obtained is $R = 0.51308$ for a fitness function value of $F = 0.79043$.

6. Comparison with Numerical Models

Two numerical models of differing complexity have been presented, based on an SPH formulation and a EMM bouncing ball representation. This section compares the experimental results presented in Section 3 with predictions from the numerical models. Such evaluations enable further physical understanding of the vertical sloshing behaviour. Figures 18, 19 and 20 show experimental and numerical trends for the acceleration envelopes and damping variation with fill level and maximum acceleration respectively. There is a good agreement between the models and experiments, particularly in the R1 region.

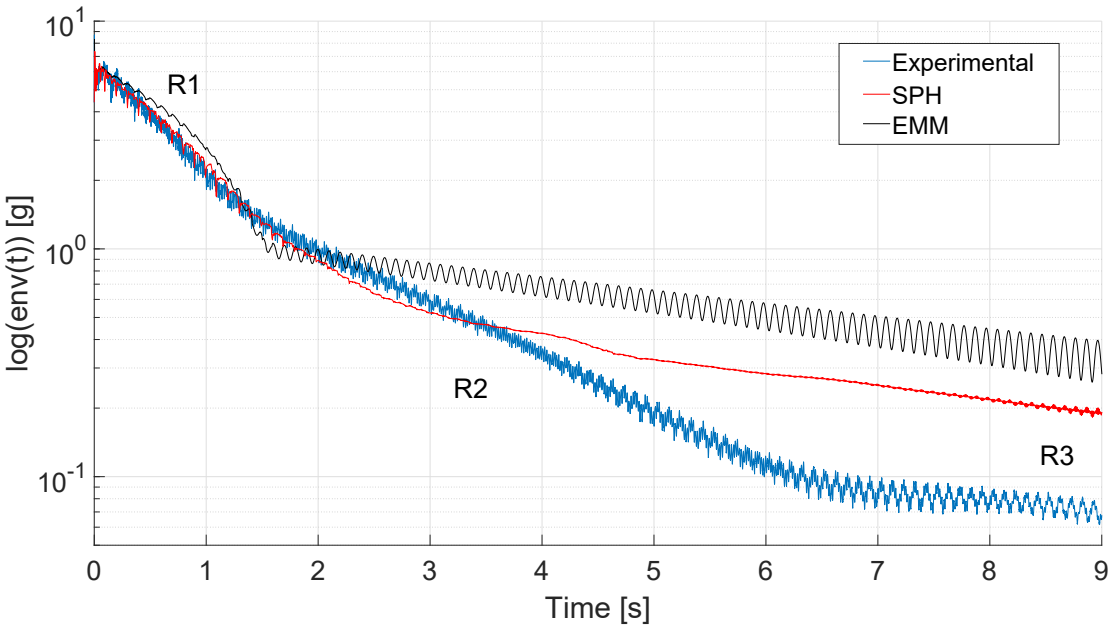

Figure 18: Acceleration envelopes for the 50% filling level case and 14 mm initial displacement, Experimental vs SPH & EMM

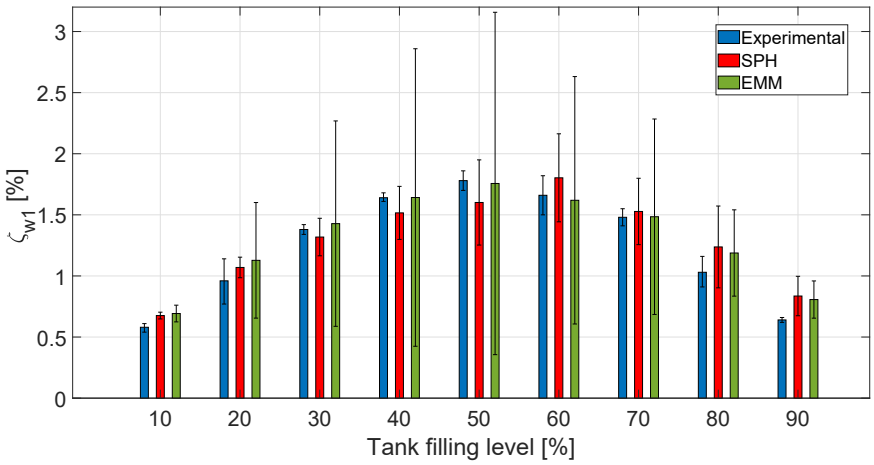

Figure 19: R1 Damping variation with fill level, Experimental vs SPH & EMM

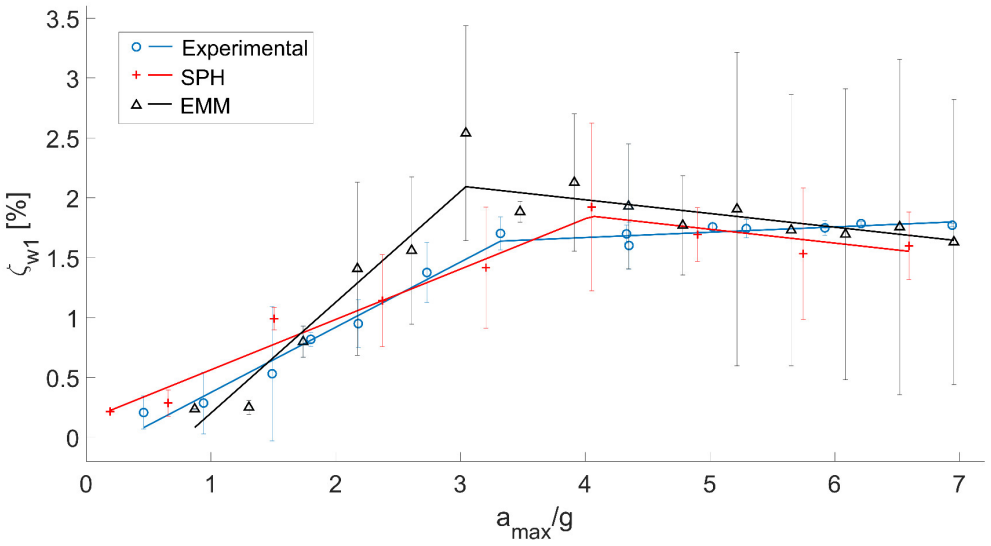

Figure 20: R1 Damping variation with maximum acceleration, Experimental vs SPH & EMM

6.1. SPH Results & Discussion

A series of SPH simulations were run to assess the experimental trends observed in section 3 and a typical acceleration response for the SPH sloshing is compared against experimental and EMM envelopes in figure 18 for the 50% fill and maximum deflection case. A sweep of simulations for varying tank filling level and initial deflection (thus maximum acceleration) was performed and the first regime damping was extracted with the relevant uncertainty boundaries and result given in figures 19 and 20. Representative snapshots of each sloshing regime are given in figure 21 which compare very well with the photos shown in figure 8.

All SPH simulations were performed on a single Intel Xeon E5-2680 v4 CPU within a dedicate compute node. For the variations in fill level, wall clock time ranged from 14 to 109 hours to achieve 10 s of simulation time.

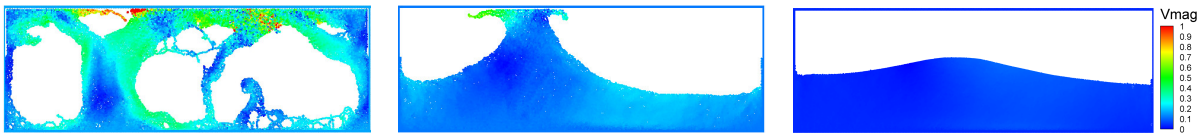

(a) R1 (b) R2 (c) R3

Figure 21: SPH snapshots of the three sloshing regimes. Colour level is velocity magnitude in m/s.

It is immediately noticeable that SPH matches the experimental response in the first regime well, with only a slight deviation from the measured behaviour, suggesting this violent impacting behaviour is relatively well resolved for the SPH and fluid-structure coupling formulation at hand. However, observation of the SPH response revealed some significant dissimilarity in the fluid behaviour itself when compared with experimental high-speed videos. Experimentally, upon release a layer of fluid originating from the meniscus is seen to rise up the side walls and impact upon the ceiling before breaking the fluid free surface. This initialises a violent, cyclic, Rayleigh-Taylor instability like behaviour in the fluid, in which water moves around cells of gas in constant collision with the upper and lower tank surfaces. This is inherently a complex multi-phase flow, with some non-negligible surface-tension effects considering the tank size. Neither of these effects are modeled in the current single-phase SPH formulation, which sees the fluid entirely separate from the lower surface upon release and a bulk impact with the top surface. Following this separation the SPH fluid breaks up, but will tend to always form a cohesive mass impacting the lower surface, as the fluid motion is uninhibited by the lack of any secondary gas phase. Inclusion of a secondary phase could thus make a significant difference on the R1 behaviour, by regulating the fluid motion into consistent impacting, rather than these

occasional impacts seen in the single-phase solutions. This consistent force would likely improve the predicted trends of the damped responses. Additionally, under strong excitation the gas may undergo significant compression, which is a source of energy dissipation and pressure loading itself. It is also worth noting that at these high Reynolds numbers strong turbulent behaviour is observed, which is not resolved with the current formulation.

The presence of the second sloshing regime is somewhat questionable in the SPH acceleration response. Instead of a clear inflection into an R2 damping region, a curved decay into the underlying structural damping (R3 region) is observed. Despite this, the fluid behaviour itself performs as expected with lateral waves oscillating at roughly 5 Hz as seen experimentally, and numerically in figure 21b. However, this first sloshing mode only occurs for roughly 3 s, compared to 5 s experimentally. This difference implies some underlying energy dissipation/interaction mechanism is missing as the fluid and structural models are individually working as expected without the fully formed combined response. This effect is most likely a result of simulating the tank in two-dimensions. Fluid behaviour seen experimentally is mostly two-dimensional due to the tank's aspect ratio, however, the interface between the fluid and tank is inherently three-dimensional. It is assumed the long side walls missing in the simulation act to drive the free-surface wave motion (which would extend the simulated response to the correct time) and provide an important underlying energy transfer mechanism. Similar behaviour will also be present during the R1 damping, although it is likely negligible compared with the violent fluid impacting. Experimentation with coarse three-dimensional simulations indeed shows the emergence of more clear R2 damping response. Unfortunately, the steep increase in cost when modelling three-dimensions means the correct resolution was not obtained in this study (50% filling scales from 15k to 2.25 million particles in 3D). Moreover, the introduction of surface tension effects in the SPH formulation is expected to lead to a better defined first symmetric sloshing mode motion, as observed experimentally; this in turn is expected to better represent the R2 sloshing region. Understanding the fluid-induced damping during the R2 regime is an ongoing area of research by the authors.

Figure 19 shows the R1 damping response with variations in fill level. SPH provides good correlation with the experimental response at lower filling levels ($< 40\%$), with any disparity mostly being within the uncertainty in damping estimation. However, damping is maximised for the 60% fill case and mostly over predicts damping at higher fill levels, similar to the EMM. High speed footage of the experimental videos shows that as filling level is increased, the motion of fluid and impacting is reduced. Instead, the fluid tends to fill the entire height of the tank, with bubbles of gas moving up and down with circulating currents inside the fluid. This physical behaviour is modelled neither in the single-phase SPH nor EMM, which describes this scenario as a large fixed mass moving vertically with small displacements, impacting the tank top and bottom surfaces.

Conversely, fluid behaviour at lower filling levels is dominated by surface tension. A majority of the fluid remains adhered to surfaces, whilst small droplets are released and free to impact. Within SPH the entire mass of fluid is free to impact the tank and thus provides the slight increase in damping. The discrepancy here is only small due to the slight differences in the moving fluid mass.

For the variations in maximum acceleration, figure 20, SPH shows very good consistency with experimental data below the saturation acceleration. Inconsistencies here are hard to define due to the small discrepancies and sensitivity of the data to damping estimation around the saturation region. However, following saturation, SPH shows a decreasing damping with increased acceleration, similar to the EMM. The cause of this is currently unknown, but it is suspected the SPH and EMM formulation lack an underlying physical mechanism that induces increased damping at larger accelerations.

Ultimately SPH provided a good prediction of the experimental results for the first violent sloshing regime. This is generally quite surprising given the simple single-phase SPH formulation, and what is quite a coarse spatial discretisation to be used within typical SPH context. Discrepancies in the response are discussed and the likely causes given. Improvements to the formulation to model a secondary gas phase, surface tension and 3D behaviour should provide an ideal fluid model to describe the sloshing. Furthermore, the simple 1DOF structural model and fluid-structure coupling scheme provided an adequate model to describe the T-Beam structure. One notable feature is that no parameter tuning was required for SPH, aside from choosing a suitable resolution. Considering the good match, SPH could be used to extrapolate the study of fluid-induced damping into other scenarios, perhaps different tank geometries or

structural models and discretisations.

6.2. EMM Results & Discussion

A series of results pertaining to the EMM modeling of the experimental results presented in section 3 are presented and discussed.

An indication of the way the EMM models the damping behaviour of a vertically sloshing system is obtained from a comparison between the acceleration envelopes. The envelopes for the 50% filling level and maximum excitation considered are presented in figure 18 for the EMM, SPH model and experimental rig. Good agreement between the EMM and the experiments is observed in regions R1 and R3. As mentioned previously, the EMM data obtained for R1 shows a deviation from the linearity of damping which generally was found to increase with the value of the coefficient of restitution. At the end of region R1 the ball stops its movement and comes to a rest relative to the moving tank, the system then transitions directly into region R3. The two mechanisms of energy dissipation present in the EMM system, as can be seen in equations 19, 20 and 21, are the underlying viscous damping of the structure (ζ in equation 19) and the momentum exchange subject to the inelastic impact condition between the bouncing ball and the vibrating tank. Damping in region R1 is thus described well by the repeated impacts between the ball and the tank floor or ceiling. Damping region R3 is naturally captured too, this being the region corresponding to virtually no relative motion between the tank and the liquid/ ball. Region R2 is not captured by this model because it is dominated by a different sloshing pattern characterised by the first symmetric sloshing mode of the liquid, as described in subsection 3.1. The damping level in R1 can be quantitatively compared between the three sets of data by using parabolic approximations of the envelope, as presented in subsection 5.2.

The R1 damping level in the experimental T-beam system was found to be maximized at a filling level of 50% and decreasing towards lower as well as higher filling levels; similar results are obtained with the EMM. A comparison between experimental and EMM results can only be made non-trivially in region R1, for reasons already discussed. The results are presented in figure 19, alongside the experimental and SPH data. The mean R1 damping, as well as the minima and maxima are presented for all of the data. A first observation is that there is little deviation from the mean R1 damping in the experimental cases, confirming the appropriateness of using a straight line fit to estimate the damping, as presented in section 3. It is apparent from figure 19 that the sloshing system's behaviour is modeled well for the 30% to 70% filling levels, with slight overestimation of damping for lower and higher filling levels. Whilst not within the scope of the present study, this observation suggests that an additional model refinement or introduction of nonlinearity in the coefficient of restitution might benefit the model's predictive capability at different filling levels.

When compared to the experimental and SPH simulations data, it is apparent that there is more deviation from the linearity of damping in the EMM model, as evident from the larger vertical bars in figure 19. While a constant slope on a logarithmic plot suggests viscous-like damping mechanism (or an exponential rate of vibration decay), the observable variation of the acceleration envelope slope suggests a different damping mechanism that appears to be dependant on the filling level, level of excitation and the value of the coefficient of restitution. These, of course, are inherent limitations when modelling complex sloshing-induced damping using a model as simple as the EMM presented here.

The damping ratio was experimentally found to only increase slightly after an excitation level above the value of $3 - 4$ g, as presented in section 3. When modelling the system using the EMM the results are found to be closer to the SPH model than to the experimental data, as the damping level in the system seems to show a slight decrease after the same excitation threshold (figure 20). These differences are most likely due to unmodeled physics on the EMM part and further investigations are needed. The vertical bars in figure 20 represent the interval between the minimum and maximum damping ratio value in R1 and show that experimentally there is less deviation from linear damping observed in R1 as compared to the EMM prediction over all acceleration values.

The behaviour of the EMM was investigated over different filling and excitation levels and the results were found to be in good agreement with both experimental and SPH data. The adequacy in modeling the behaviour of the

experimental setup and the results obtained were satisfactory especially considering the simplicity of the EMM; the model shows certain limitations nevertheless, and further work is needed in order to model the sloshing-induced damping more precisely.

7. Conclusions

An experimental study has been performed to investigate the effect of vertical sloshing on the transient damping behaviour of a single degree of freedom T-beam system attached to a tank containing variable amounts of liquid and subjected to different levels of motion. The presence of the fluid significantly increases the inherent damping in the system, but this is dependent upon the filling level of the tank and the size of motion. The maximum amount of damping was achieved at a 50% fill level and the system showed three distinct piece-wise linear damped response regimes during the transient decay, all related to different motions of the fluid. The first response regime, immediately at the start of the transient, is considered to be the most important to exploit for aircraft gust loads alleviation; its damping level is found to be more or less constant after an excitation level threshold is met. The experimental tests were compared with numerical simulations using two different fidelity approaches, smoothed particle hydrodynamics and an equivalent mechanical model based upon a bouncing ball, to model the fluid motion. All modelling methods gave a reasonable representation of the experimental results, particularly for the initial damping zone.

The results presented in this work demonstrate the effectiveness of various sloshing-induced damping mechanisms to reduce the dynamic response in vertically vibrating structures and the ability to model the most significant phenomenon. This study is seen as a first step in understanding the possibility of exploiting and enhancing the wing – fuel dynamic interactions as a means to achieve aircraft passive loads alleviation.

Acknowledgement

The research leading to these results was undertaken as part of the SLOWD project which has received funding from the European Union's Horizon 2020 research and innovation programme under grant agreement No. 815044. The SPH numerical work was carried out using the computational facilities of the Advanced Computing Research Centre, University of Bristol - http://www.bris.ac.uk/acrc/ and the assistance of Mr Adrian Kraft is gratefully acknowledged.

References

[1] J.R. Wright, J.E. Cooper, *Introduction to Aircraft Aeroelasticity and Loads*, 2nd Edition, John Wiley, 2014.
[2] O. Stodieck, J.E. Cooper, P.M. Weaver, P. Kealy, *Aeroelastic Tailoring of a Representative Wing Box Using Tow-Steered Composites*, AIAA Journal Vol. 55, No. 4, pp 1425 - 1437, April 2017
[3] Castrichini, A, V. H. Siddaramaiah, D. Calderon, J.E. Cooper, T. Wilson, Y. Lemmens, *Preliminary investigation of use of flexible folding wing tips for static and dynamic load alleviation*, Aeronautical Journal, Vol. 121, No. 1235, pp 73-94, January 2017.
[4] B. Bouscasse, A. Colagrossi, A. Souto-Iglesias, J.L. Cercos-Pita, *Mechanical energy dissipation induced by sloshing and wave breaking in a fully coupled angular motion system. I. Theoretical formulation and numerical investigation*. Physics of Fluids, 26(3), 2014
[5] B. Bouscasse, A. Colagrossi, A. Souto-Iglesias, J.L. Cercos-Pita, *Mechanical energy dissipation induced by sloshing and wave breaking in a fully coupled angular motion system. II. Experimental investigation*, Physics of Fluids, 26(3), 2014
[6] US Patent US4724923A, *Vibration absorber with controllable resonance frequency*, 1986
[7] US Patent US20130092489A1, *Aeroelastic tuned mass damper*, 2011
[8] J. Hall , T.C.S. Rendall, C.B. Allen, H. Peel, *A multi-physics computational model of fuel sloshing effects on aeroelastic behavior*, Journal of Fluids and Structures, 56, 11 – 32, 2015
[9] R.D. Friend, V.K. Kinra, *Particle Impact Damping*, Journal of Sound and Vibration 233(1), 93-118, 2000
[10] H.N. Abramson (Ed.), *The Dynamic Behavior of Liquids in Moving Containers, with Applications to Space Vehicle Technology*, Chapter 8 - Vertical Excitation of Propellant Tanks, NASA-SP-106, 1966
[11] R.A. Ibrahim, A. Soundararajan, *Non-linear parametric liquid sloshing under wide band random excitation*, Journal of Sound and Vibration 91(l), 119-134, 1983
[12] R.A. Ibrahim, R.T. Heinrich, *Experimental Investigation of Liquid Sloshing Under Parametric Random Excitation*, Journal of Applied Mechanics, Vol. 55, June 1988
[13] A. Agneni, L. Balis-Crema, *Damping measurements from truncated signals via Hilbert transform*, Mechanical Systems and Signal Processing, 3(1), 1-13, 1989
[14] J.E. Cooper, P.R. Emmett, J.R. Wright, *Envelope function - A tool for analyzing flutter data*, Journal of Aircraft, Vol. 30 No. 5, 1993

[15] F. Gambioli, R.A. Usach, J. Kirby, T. Wilson, *Experimental Evaluation of Fuel Sloshing Effects on Wing Dynamics*, International Forum on Aeroelasticity and Structural Dynamics, June 2019
[16] B. Titurus, J.E. Cooper, F. Saltari, F. Mastroddi, F. Gambioli, *Analysis of a Sloshing Beam Experiment*, International Forum on Aeroelasticity and Structural Dynamics, June 2019
[17] H. Lamb, *Hydrodynamics*, 6th Edition, Cambridge University Press, 1953
[18] R.A. Ibrahim, *Liquid Sloshing Dynamics Theory and Application*, Cambridge University Press, 2005
[19] S.S Rao, *Mechanical Vibrations*, Pearson, 6th Edition, 2016
[20] G. Popov, T.S. Sankar, G.H. Vatistas, *Dynamics of Liquid Sloshing in Horizontal Cylindrical Road Containers*, Proceedings of the Institution of Mechanical Engineers, Part C: Journal of Mechanical Engineering Science, 207(6), 399–406, 1993
[21] I.M. Ibrahim, *Anti-Slosh Damper Design for Improving the Roll Dynamic Behavior of Cylindrical Tank Trucks*, SAE Transactions Vol. 108, Section 2: JOURNAL OF COMMERCIAL VEHICLES, pp. 535-541, 1999
[22] V.N Pilipchuk, R.A. Ibrahim, *Dynamics of a Two-Pendulum Model with Impact Interaction and an Elastic Support*, Nonlinear Dynamics volume 21, pp 221–247, 2000
[23] M.Farid, O.V. Gendelman, *Response regimes in equivalent mechanical model of strongly nonlinear liquid sloshing*, International Journal of Non-Linear Mechanics Volume 94, pp 146-159, September 2017
[24] L. B. Lucy, *A numerical approach to the testing of the fission hypothesis*, Astronomical Journal, vol. 82, 1977.
[25] R. A. Gingold and J. J. Monaghan, *Smoothed particle hydrodynamics - theory and application to non-spherical stars*, Monthly Notices of the Royal Astronomical Society, vol. 181, 1977.
[26] C. Hirt and B. Nichols, *Volume of fluid (vof) method for the dynamics of free boundary*, Journal of Computational Physics, vol. 39, 01 1981.
[27] J. Monaghan, *Smoothed particle hydrodynamics and its diverse applications*, Annual Review of Fluid Mechanics, vol. 44, 2012.
[28] D. J. Price, *Smoothed particle hydrodynamics and magnetohydrodynamics*, Journal of Computational Physics, vol. 231, no. 3, pp. 759 – 794, 2012, special Issue: Computational Plasma Physics.
[29] G. R. Liu and M. B. Liu, *Smoothed Particle Hydrodynamics, a meshfree particle method*. World Scientific, 2003.
[30] J. J. Monaghan, *Smoothed particle hydrodynamics*, Annual review of astronomy and astrophysics, vol. 30, 1992.
[31] J. P. Morris, P. J. Fox, and Y. Zhu, *Modeling low reynolds number incompressible flows using sph*, Journal of Computational Physics, vol. 136, no. 1, pp. 214 – 226, 1997.
[32] X. Xu and X.-L. Deng, *An improved weakly compressible sph method for simulating free surface flows of viscous and viscoelastic fluids*, Computer Physics Communications, vol. 201, pp. 43 – 62, 2016.
[33] A. Crespo, M. Gómez-Gesteira, R. A. Dalrymple *et al.*, *Boundary conditions generated by dynamic particles in sph methods*, CMC-TECH SCIENCE PRESS, vol. 5, no. 3, p. 173, 2007.
[34] R. H. Cole, *Underwater explosions*. Princeton University Press, Princeton, 1948.
[35] J. Monaghan, *Simulating free surface flows with sph*, Journal of Computational Physics, vol. 110, no. 2, pp. 399 – 406, 1994.
[36] H. Wendland, *Piecewise polynomial, positive definite and compactly supported radial functions of minimal degree*, Advances in Computational Mathematics, vol. 4, no. 1, pp. 389–396, Dec 1995.
[37] F. Macià, A. Colagrossi, M. Antuono, and A. Souto-Iglesias, *Benefits of using a wendland kernel for free-surface flows*, 6th ERCOFTAC SPHERIC Workshop on SPH Applications, pp. 30–37, 01 2011.
[38] N. M. Newmark, *A method of computation for structural dynamics*, Journal of the Engineering Mechanics Division, vol. 85, 1959.
[39] J. Calderon, L. González, S. Marrone, A. Colagrossi and F. Gambioli, 2019. *A SPH simulation of the sloshing phenomenon inside fuel tanks of the aircraft wings*. In: Proceedings of the 14th SPHERIC International Workshop, Exeter, UK. pp. 106-113.
[40] Pilipchuk, V.N. and Ibrahim, R.A., *The dynamics of a non-linear system simulating liquid sloshing impact in moving structures*, Journal of Sound and vibration, Vol.205, No.5, pp.593-615, 1997.
[41] Ibrahim, R.A., *Assessment of breaking waves and liquid sloshing impact*, Nonlinear Dynamics, pp.1-89, 2020
[42] Godderidge, B., Turnock, S.R. and Tan, M., *A rapid method for the simulation of sloshing using a mathematical model based on the pendulum equation*, Computers & Fluids, Vol.57, pp.163-171, 2012